Computers in Biology and Medicine 104 (2019) 10–28

Contents lists available at ScienceDirect

Computers in Biology and Medicine

journal homepage: www.elsevier.com/locate/compbiomed

A new nonparametric statistical approach to detect lumen and Media-Adventitia borders in intravascular ultrasound frames

Ali Kermani, Ahmad Ayatollahi*

School of Electrical Engineering, Iran University of Science and Technology, Iran

ARTICLE INFO

Keywords:
Intravascular image
Ultrasound
Border detection
Nonparametric statistics
Cubic spline

ABSTRACT

Intravascular ultrasound (IVUS) imaging is widely known as a powerful interventional imaging modality for diagnosing atherosclerosis, and for treatment planning. In this regard, the detection of lumen and media–adventitia (MA) borders is considered to be a vital process. However, the manual detection of these two borders by the physician is cumbersome due to the large number of frames in a sequence. In addition, no approved universal automatic method has been presented so far due to the great diversity in the appearance of the coronary artery in the images acquired by different IVUS systems. To this end, the present study aimed to provide a new border search theory on the radial profile, based upon the nonparametric statistical approach, and to develop a generic and fully automatic three-step process for extracting the lumen and MA borders in IVUS frames based on the proposed theory. Thereafter, the proposed theory and three-step process were evaluated on synthetic images, as well as on a test set of standard publicly available images, respectively. The results showed that our three-step process could segment the borders with ≥ 0.82 and with ≥ 0.75 Jaccard measure (JM) to manual borders in IVUS frames acquired by the 20 MHz and 40 MHz probes, respectively. Based on the results, the lumen and MA borders can be extracted automatically, and the border extraction process can be implemented in parallel for a polar image due to the capability of the present proposed method to estimate the borders for each angle independently.

1. Introduction

Today, producing catheter and intravascular ultrasound (IVUS) imaging system is currently known as the gold standard of in-vivo intravascular imaging for the vessel wall interrogation even after 40 years when it was suggested by Bom et al. [1,2]. In addition to providing quantitative information such as the luminal Cross-Sectional Area (CSA), abluminal CSA, atheroma CSA, and vascular remodeling, IVUS is widely used for evaluating important qualitative information such as atheroma morphology, intervention outcome, and plaque progression [3]. Further, IVUS can lead to improved results in the process of diagnosis and percutaneous coronary interventions as a complementary and adjunctive module, along with X-ray angiography [4].

The IVUS image provides the cross-sectional view of the coronary artery, the quality of which is evaluated by spatial and contrast resolution [3,5]. The transducer frequency is one of the most effective factors in the two above-mentioned resolutions. A cross-section of the coronary artery often consists of three layers [3]. The innermost layer is composed of three tissues including atheroma (patient vessels), intima, and internal elastic membrane (IEM). Regarding echogenic properties, this layer is more separable in IVUS images than the lumen area [3]. The middle layer is composed of media and external elastic membrane (EEM), which is usually darker in the image since it is less echogenic than the internal layer. The outermost layer encompasses adventitia and periadventitial and is typically brighter than the middle layer [3]. In addition, the artifact factors such as guidewire artifact, non-uniform rotational distortion, and discontinuity at 0° [5]), and vessel morphology like plaque, bifurcation, and stent [6]) can considerably affect the appearance of the IVUS image. The aforementioned factors associated with the quality and the appearance of the IVUS image causing the segmentation of the IVUS image, especially the separation of the internal and external layers have been regarded as a challenge. Further, the (semi-)automatic segmentation methods have been emphasized for time-saving, as well as overcoming the inter- and intra-observer variations since an imaging process yields a large number of the IVUS frames.

Regarding the classification of (semi-)automatic IVUS image segmentation methods, the direct detection of the borders is considered as one of the major categories [5]. In this category, the recent approaches are mostly classified under the machine learning-based methods,

* Corresponding author. School of Electrical Engineering Iran, University of Science and Technology(IUST), Narmak, Tehran, 16844, Iran.
E-mail address: ayatollahi@iust.ac.ir (A. Ayatollahi).

https://doi.org/10.1016/j.compbiomed.2018.10.024
Received 18 June 2018; Received in revised form 20 October 2018; Accepted 23 October 2018
0010-4825/

deformable model-based methods, border and gradient tracking-based methods, as well as statistical and probabilistic techniques, which will be reviewed here (see Refs. [5–7] for further studies on the methods published before 2014).

In machine learning-based methods, the holistic approach was introduced by Ciompi et al. [8] for extracting the MA. In this method, border detection and refinement are done in parallel. Border detection is performed through multi-scale stacked sequential learning and holistic algorithm, while border refinement is done by implementing a matched filter. In Ref. [9], a support vector machine classifier was used for segmenting non-artifact images by evaluating a large group of features, and selecting the noise reduction filters and Haralick's textural features as the most effective features. In another study, an ANN-based hierarchical algorithm was proposed to extract the lumen and MA borders [10]. In this method, the lumen and MA borders are estimated by utilizing double ANN (DANN) after blurring the IVUS image. Finally, the active contour is used for smoothing the final borders. In Ref. [11], a three-step circulatory index-based automatic method was proposed to extract the lumen border of images acquired by the 20 MHz probes in the absence of other artifacts. The preprocessing includes noise elimination and contrast improvement. The segmentation procedure is performed by using k-means, along with subtractive clustering, followed by detecting and eliminating the bifurcation regions. In the third step, the convex hull structure technique, circulator index, and active contour are used to estimate the final smooth lumen border. The deformable model was used with different initialization techniques in order to detect the lumen and MA borders [12,13]. In Ref. [12], after preprocessing the removal of the catheter artifact, an active contour model, along with threshold-based initialization and maximum brightness, was proposed for automatic extraction of the lumen and MA borders for IVUS images with 40 MHz probes. Zakeri et al. [13] proposed a fourfold deterministic statistical strategy for MA border extraction in the images with 30 MHz probes in the absence of most of the artifacts. In the first phase, a sparse binary image was created by using the local appearance model, followed by creating a new dynamic external force pattern of the sparse binary image. The initial contour was extracted by multiplying the two obtained images. The second phase involved smoothing the initial contour. During the third phase, an active contour was used to estimate the MA border. In addition, during the fourth phase, called “ad-hoc”, the shadowing and calcification regions are revealed and pruned at the border and. The use of image gradient and border tracking was proposed in Refs. [14–16], respectively. In Ref. [14], fast marching method (FMM), which combines the edge contour information with region information, was proposed for extracting the lumen and MA borders. The edge contour information was obtained by proposing a new speed function based on the textural gradient, and the region information was obtained through gamma modeling for the IVUS image texture. This algorithm requires an initial contour between the lumen and intima, as well as an initial contour between the media and adventitia in the IVUS longitudinal-mode image. This method was evaluated by means of a complete database including different kinds of vessels. In Ref. [15], a two-stage process made from the shape prior model was proposed based on the node-weighted directed graph to extract the lumen and MA borders. During the first stage, a prior border was estimated by minimizing the cost function. The second stage included estimating the border location, correcting the arc of the nodes corresponding to the borders, and minimizing the adapted graph energy. The cost function used in this method was designed based on the random forest classifier with respect to the image texture and artifact, which required training. By approving the efficiency of extremal regions in extremum levels (EREL) detector in border detection, Faraji et al. [16] proposed an algorithm based on this detector, along with the ellipse fitting algorithm for extracting the lumen and MA borders in the IVUS images. EREL is a new region detector, which uses the union-find sets related to the edge information, to detect a series of unified pixels in the image. In this method, the selection of the appropriate EREL has become a local maxima searching (LMS) problem, which can be resolved by measuring a series of textural characteristics for each EREL and defining a texture score. The quantitative comparison of this method could confirm its success only in the absence of artifacts for images acquired by the 20 MHz probes. The statistical methods were proposed by Unal et al. [17] and China et al. [18]. Further, the shape modeling of the lumen and adventitial borders were used in Ref. [17], which necessitates the training of the model with prior images. The nonparametric light intensity, along with global image measurements, was proposed for extracting lumen border. Furthermore, an oriented-smooth gradient was developed for MA border extraction. In addition, two ad-hoc processes were proposed for detecting calcification and bifurcation. Further, the use of multiscale random walks was proposed for extracting the lumen and MA borders in Ref. [18]. This procedure is performed in three steps including the estimation of signal confidence, the initialization of contour border by using joint learning of extraction, and the use of random walks for extracting the final smooth border. This method requires labeled data for training.

By considering the above-mentioned methods, the previous works had at least one of the limitations such as the need for training and initialization, responsiveness in normal artery image or in images with minimum artifacts, applicability only for images with a certain probe frequency, as well as the need for global or local processing, which leads to the limited possibility of parallel optimization of the algorithm procedure. Thus, it is essential to design a universal automatic method with the capability of the parallelization, along with standard evaluation. To this end, the present study aimed to provide a single-frame universal method with minimal dependency on the global image. It was hypothesized that the artery wall boundaries may be extracted in a cross-sectional image at each angle independently since the IVUS image is produced from a combination of radio frequency signals, along with some post-processing methods. In other words, presenting a new statistical theory of radial border extraction called “radial threshold”, and developing a border extraction procedure for the IVUS frames were considered as the main objectives. In this regard, a theory of border estimation on the radial profile based on the nonparametric statistical approach is proposed to provide an independent border extraction process at each cutting angle. In addition, the conventional analysis of variance (ANOVA) criterion is improved by a regularization term with respect to the features of the IVUS image. After presenting the theory, a simple process based on this theory is proposed for extracting the lumen and MA borders in an IVUS frame. This process consists of three main steps. In the first step, the method introduced by Ref. [17] is improved for removing the effect of the catheter artifact in order to make this algorithm independent from the frame sequence. During the second step, a sequential algorithm is obtained for estimating the lumen and MA borders. Finally, an ad-hoc is provided for detecting and correcting discontinuous borders. The evaluation procedure is performed based on two datasets. First, the synthetic images with added speckle noise are used to approve the proposed theory. Then, the three-step process of border detection is evaluated by using the test set of standard publicly available dataset [6] in order to provide the ground for a fair comparison with other previous studies.

The rest of this paper is organized as follows. Section 2 presents the IVUS synthetic images and the dataset used in this research, explains the preliminaries for the theory, represents the theory, and proposes a theory-based process, respectively. Section 3 provides the evaluation results of the proposed theory, as well as the proposed process. Section 4 highlights the strengths and weaknesses of the proposed process. Finally, the conclusions are provided in Section 5.

2. Materials and method

2.1. Materials

The present study was conducted by using two image datasets. The first set includes synthetic images containing the speckle noise. The structure of these images is similar to the IVUS image. The speckle noise is added to the primary image using a general model for the speckle noise given by Ref. [19]:

$$I_{speckled} = I + n \times I \quad (1)$$

where I indicates the input raw image and n represents the random noise with uniform distribution, mean 0, and standard deviation v. The value of standard deviation v is such initialized that a wide range of PSNR can be obtained.

The second set includes the publicly available data introduced for a challenge [6] (http://www.cvc.uab.es/IVUSchallenge2011/dataset.html). In this data collection, clinical recordings are in such a way that they can cover various conditions including different types of plaques such as lipidic, fibrotic and calcified plaques, as well as different morphologies of the coronary such as the presence of bifurcation, shadows, proximity of the probe to the vessel. Due to the large number of frames in an IVUS pullback, a subset of significant frames was extracted in order to involve minimum consecutive frames to support the state-of-the-art segmentation algorithms [6]. The data collection consisted of two datasets:

Dataset A: This dataset includes 77 single frames of the in-vivo coronary arteries taken from 22 different patients by using an iLab IVUS -Boston Scientific device, equipped with a 40 MHz Atlantis SR 40 Pro catheter. These data features represented a good diversity of artifacts, especially a frame without any artifact or plaque, 7 frames containing plaques but no artifacts, 16 frames with bifurcation, 22 frames with stent, 8 frames with side vessel, 42 frames with shadow artifact, 36 frames with artificial effect of guidewire, and 39 frames with catheter touching the lumen (some frames included multiple artifacts). In addition, all of these frames included ring-down artifact and calibration square. Further, the average (standard deviation) measure of lumen and media areas, and stenosis degree were 10.62 (5.62) mm^2 and 18.27 (6.70) mm^2, and 57%(14%), respectively.

Dataset B: This dataset included 435 frames of the in-vivo coronary arteries taken from 10 different patients by using a Si5-Volcano Corporation device, equipped with a 20 MHz Eagle Eye monorail catheter. In addition, this dataset encompasses 20-50-successive-frame sequences. Further, it involves less artifact diversity than dataset A. Particularly, the dataset consists of 225 frames without artifacts, 60 with bifurcation, 94 containing side vessel, and 106 with shadow artifact (some frames included multiple artifacts simultaneously). It is worth noting that all the frames in this dataset contained plaques. Furthermore, unlike dataset A, the frames of dataset B are devoid of ring-down artifact and calibration square. In addition, the mean (standard deviation) measure of lumen and media areas, and stenosis degree are 8.68 (3.23) mm^2 and 15.59 (4.47) mm^2, and 54% (9%), respectively.

In addition, the images were independently annotated by four experts for both lumen and MA borders in both datasets A and B. The experts were all physicians. They worked daily with the specific IVUS imaging system, and were related to the different medical centers [6]. Further, two of the experts repeated their annotations after a week [6].

In the next procedure, each of the two datasets (A and B) was divided into training and test sets. One-quarter of each dataset was selected as the training set and another three-quarter were regarded as the test set. In this study, the test set of datasets including 58 and 326 IVUS B-mode images was respectively used for dataset A and B.

2.2. Theory preliminaries

Otsu's technique [20] is considered as the most well-known threshold-based segmentation method, which is based on the between-class variance at gray levels. However, a large number of researchers have developed the method due to its limitations. The within-class variance (WCV) at gray levels is a method proposed for overcoming the limitation of the presence of bias at the threshold value for the non-uniform distribution of gray levels in image regions [21]. On the other hand, in addition to the gray level information, the spatial distribution of the gray levels is very effective in segmentation, which was ignored in Otsu's method. The two-dimensional (2-D) thresholding was introduced as the main solution for adding the spatial information to the segmentation procedure [22] although it involves considerable computational loads [22]. Therefore, in order to reduce the computational load while establishing the result's reliability, the extended thresholding was proposed, along with the fast 2-D thresholding [23]. In this method, the 2-D density function maps to a one-dimensional function.

Based on the experimental results, there are some parameters causing the limitations in all the Otsu-based segmentation methods such as small object size, small mean difference between the objects, large variance of the objects, and low SNR of the image [24]. During the past decade, researchers have focused on eliminating any limitation of Otsu's method with respect to their own specific segmentation purpose. Accordingly, the segmentation of a small object (defect) by scaling Otsu's primary criterion is regarded as one of the proposed methods in this regard [25,26]. By adding a comparative complementary term to Otsu's primary criterion, the problem of segmenting large-variance objects was resolved [27].

However, most of the above-mentioned limitations coincided with ultrasound imaging in its global state. Therefore, the Otsu's approach cannot yield reliable results for the global state of ultrasound images, except for specific cases. A specific case includes the cases in which at least one of the intended objects is homogenous or the objects have the same dimensions [28]. However, these two prerequisites do not necessarily occur in the IVUS images since higher levels of correlation are negligible and occur only in dense objects such as a calcified region and the regions of interest (ROI) are commonly smaller than the background in the IVUS images. In this regard, some researchers used the Otsu's approach as a preprocessing for IVUS image segmentations. Sofian et al. [29] detected the MA boundary by using a threshold based method and implemented the Otsu's approach, along with an empirical thresholding and the binary – morphological operations. However, this method cannot be performed generally due to the use of empirical thresholding.

According to the Otsu's approach, the dependence of the approach on the single brightness intensity distribution, and the analysis of variance (ANOVA) criterion are considered as the main reasons for such an event. Subsequently, the prior suggestions are provided for each of the cases by presenting the specifications and features found in the IVUS images.

In addition, the brightness intensity distribution in the IVUS images strongly depends on the position of the pixels. For example, Fig. 1(a) illustrates a 40 MHz IVUS frame, along with the brightness intensity distribution of the whole image (no highlight), lumen region (red highlight), and media region (green highlight). As shown, defining the brightness intensity distribution function for a spatial range (spatial threshold) may reveal significant difference in the densities although the global brightness intensity distribution has no clear separation points in order not to extract different textures by the intensity thresholding. By considering the catheter structure in the IVUS imaging, the spatial dependence of the brightness intensity distribution of a frame can be summarized to the radius and angle variables [30,31]. Regarding the IVUS sequential angular imaging, the present study aimed to limit the texture border search space to each angle because the problem of searching for the texture border is converted into finding the appropriate radius at each angle in such a case as displayed at Fig. 1 (a)

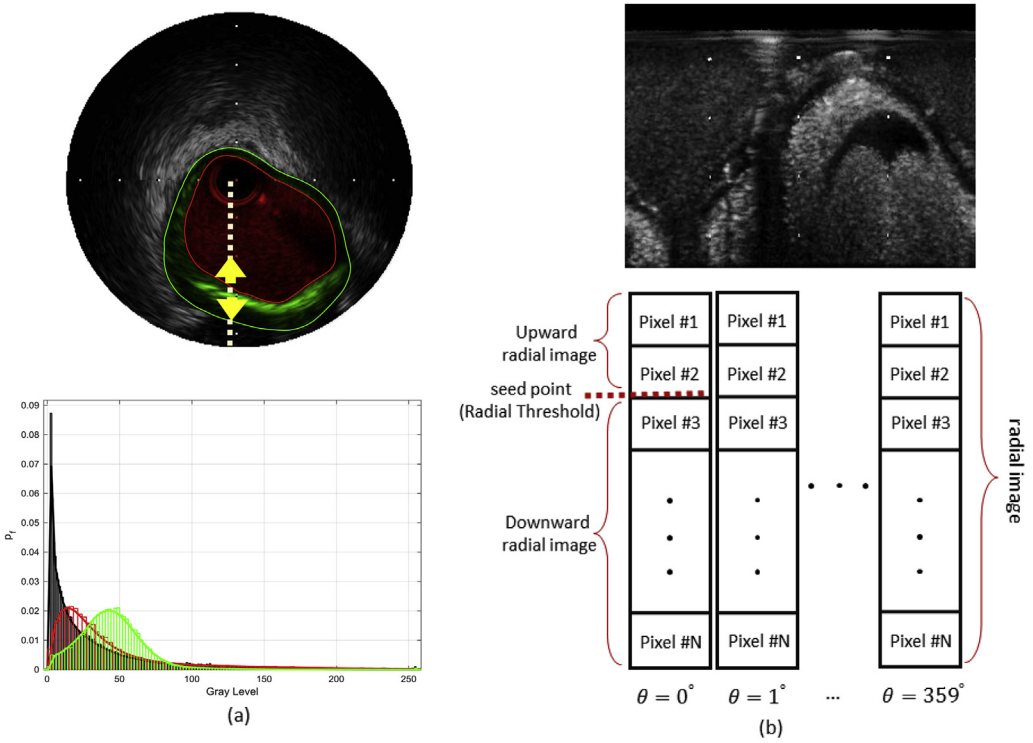

Fig. 1. (a) A 40 MHz IVUS frame [6] with intensity distribution of the global image (no highlight), intensity distribution of lumen area (red highlight), intensity distribution of media area (green highlight); (b) IVUS polar image as a set of the radial images and selection of the seed point.

in yellow arrows. Further, it is considered as the main idea in the present work, i.e. the estimation of a radial threshold for the radial distribution of the brightness intensity at a certain angle.

In the present study, assuming the use of WCV (equality of weighted class variances or equality of dimensions [28]), as well as the incompatibility with the IVUS image, it was proposed to improve the WCV criterion by a regularization term embracing the extent of equality of WCV.

2.3. Primary definitions used in theory

In the proposed theory, the polar image is defined as a set of the radial images (Fig. 1(b)) and a set of the radial discrete points (known as seed points) is considered for each angle. Here, the angle resolution of radial images named "search zone box" is 1°. For each seed point, the radial image is divided into two parts in the upward and downward directions. Table 1 indicates the variables in these two parts of the radial image, along with the definition of each of them. Further, the following notations are used:

$$P_A = P(A)\ ;\ \textit{Probabilty of } A \tag{2}$$

$$P_B^A = P(B|A)\ ;\ \textit{the conditional probability of } B \textit{ given } A \tag{3}$$

Table 1
The list of the variables used in the radial image as well as their definitions.

Variable	Definition
RI	Radial Image
N	Total number of pixels in RI
N_{up}	Total number of pixels in upward of RI
N_{dn}	Total number of pixels in downward of RI
n_i^R	Number of pixels at level *i* intensity in RI
n_i^k	Number of pixels at level *i* intensity in upward of RI

2.4. Radial threshold theory

It is assumed that each pixel of the radial image has L different gray levels ([1,…,L]). In addition, each radial image has R different discrete radii, known as seed points ([1,…, R]). Further, a normalized histogram is used to calculate the gray level probability distribution function in the radial image. The occurrence probability of brightness intensity ***i*** in the radial images is calculated as follows:

$$P_i = \frac{n_i^R}{N} \tag{4}$$

Now, the radial image is segmented into the upward and downward classes by selecting a seed point ***k***. The following equation is obtained by using the conditional probability law for the upward class:

$$P(C_{up}) = P_i^{up} = \frac{n_i^k}{N_{up}} = \frac{n_i^k}{k} = P_i^k \tag{5}$$

Similarly, equation (6) is used for the downward class:

$$P(C_{dn}) = P_i^{dn} = \frac{n_i^R - n_i^k}{N-k} = \frac{N}{N-k}P_i - \frac{k}{N-k}P_i^k \tag{6}$$

where C_{up} indicates the pixels in the radial discrete position [0,1, …, k] and C_{dn} represents the pixels in the radial discrete position [k + 1, …, R]. The mean of the classes is as follows:

$$\mu_{up}(k) = \sum_{i=1}^{L} i\, P_i^{up} = \sum_{i=1}^{L} i\, \frac{n_i^k}{k} = \frac{M(k)}{P(k)} \tag{7}$$

$$\mu_{dn}(k) = \sum_{i=1}^{L} i\, P_i^{dn} = \sum_{i=1}^{L} i\, \frac{n_i^R - n_i^k}{N-k} = \frac{M(R) - M(k)}{1 - P(k)} \tag{8}$$

where *M(k)* is the first-order cumulative moment of the distribution of class *k*:

$$M(k) = \sum_{i=1}^{L} i\, \frac{n_i^k}{N} \tag{9}$$

and *P(k)* is the occurrence probability of class *k*:

$$P(k) = \frac{k}{N} \tag{10}$$

Further, the variance of the classes is used as follows:

$$\sigma_{up}^2(k) = \sum_{i=1}^{L} (i - \mu_{up})^2 P_i^{up} = \sum_{i=1}^{L} (i - \mu_{up})^2 \frac{n_i^k}{k} \tag{11}$$

$$\sigma_{dn}^2(k) = \sum_{i=1}^{L} (i - \mu_{dn})^2 P_i^{dn} = \sum_{i=1}^{L} (i - \mu_{dn})^2 \frac{n_i^R - n_i^k}{N - k} \tag{12}$$

In order to evaluate relative dispersion of the classes, the individual class variance weighted by its respective class probability is used as follow [32]:

$$\sigma_w^2 = w\sigma^2 \tag{13}$$

where *w* represents the class probability ($P(k) = {}^{k}/_{N}$ and *1-P(k)*, especially in the present study).

Regarding the limitations of ANOVA, it is proposed to add a regularization term to the WCV in order to control the changes in WCV and preserve the initial condition of the ANOVA to achieve a desirable threshold *k*:

$$\sigma_{RWCV}^2(k) = \lambda\sigma_w^2(k) + (1 - \lambda)\sigma_d^2(k) \tag{14}$$

where

$$\sigma_w^2(k) = P(k)\sigma_{up}^2(k) + [1 - P(k)]\sigma_{dn}^2(k) \tag{15}$$

is the WCV criterion, and

$$\sigma_d^2(k) = |P(k)\sigma_{up}^2(k) - [1 - P(k)]\sigma_{dn}^2(k)| \tag{16}$$

is named “differential variance”. Compared to other regions in the radial image, more changes around a border leads to closer values of the upward and downward weighted variances, which results in creating smaller differential variance. λ ranged within *[0,1]* is considered as the weighting parameter. In the present study, the value of $\lambda = 0.5$ was selected (refer to Section 3.2).

The optimal *k* value, which leads to the smallest σ_{RWCV}^2 value, can be obtained by a sequential search structure for the interval of [1,…,R]:

$$k^{opt} = \underset{k\in[1.....R]}{\operatorname{argmin}} \{\sigma_{RWCV}^2\} \tag{17}$$

In addition, this theory can be generalized to the images with the multiple textures, which can be accomplished by repeating the search for the upward and downward parts of the k^{opt} point obtained from the previous step.

2.5. Proposed border detection process

Fig. 2 displays different steps of the proposed border detection process as detailed in the following subsections.

2.5.1. Preprocessing

The image is converted from Cartesian coordinates into Polar coordinates since the structure of the proposed algorithm is based on two parameters of radius and angle in the image in the most basic step. The polar image is named I_{pol}. In addition, this conversion includes two other advantages such as automatic removal of the image area with a radius larger than the effective imaging depth, and the possibility of simple removal of the position of the catheter and its artifact in the image by knowing the appropriate radius.

The calibration square artifact is regarded as one of the artifacts in the IVUS images, which causes errors in estimating the correct border. Such an artifact can be removed by using the feature of this square in the image. These positions in the image have the maximum brightness intensity for the number of bits per pixel. Therefore, the calibration square in the image is removed by replacing the number of pixels with maximum brightness intensity with the global image mean:

$$I_{pol}\left(\underset{r.\theta}{\arg}(I_{pol} = 2^n - 1)\right) = \frac{1}{M \times N} \sum_{\substack{0\le i \le M \\ 0<j<N}} I_{pol}(i.j) \tag{18}$$

where M and N indicate the dimensions of the image in the polar coordinates and n represents the number of bits per pixel.

Further, the optimized version of the technique in Ref. [17] is used to estimate the radius of catheter artifact. First, the algorithm should be changed in such a way that, in case of the presence of no catheter artifact, only the actual diameter of the catheter is removed and mistaken removal of the lumen area (false positive) is minimized since it is used to evaluate the generality of algorithm. For this purpose, in the polar image, the minimum radius with non-zero brightness intensity in the whole image and the value of brightness intensity for all the angles in the image are set equal to the maximum brightness intensity of the image:

$$I_{pol}(r_{min}.\ \theta) = \max(I_{pol}) \text{ for } \theta = [0.360) \tag{19}$$

where,

$$r_{min} = \min\left(\underset{r}{\arg}(I_{pol} \neq 0)\right) \tag{20}$$

Second, a frame with the rotation of the same frame relative to the catheter center is used as the algorithm input in Ref. [17] instead of considering a series of consecutive frames as the input. In other words, an image with the distinct contrast between the artifact and non-artifact pixels is created by calculating the global minimum between the image itself and the rotated images, due to the circularity of the catheter artifact in Cartesian coordinates. The rotation action in the Cartesian coordinates is equivalent to the shift of the same image in the Polar coordinates. Therefore, in order to calculate the global minimum between the image and rotated images, we have:

$$I_{min}(r\ .\ \theta) = \min_{i=k\Delta\varphi\ \ \forall\ k\in\left[0.\frac{360}{\Delta\varphi}\right)} I_{pol}^i\left(r.\ \theta\right) \tag{21}$$

where I_{pol}^i represents the image shifted in polar coordinates by ***i***. In this study, the rotation angle step $\Delta\varphi$ was selected equal to 18°. Fig. 3 illustrates the removal steps of the calibration square artifact, as well as estimating the radial position of the catheter artifact and its removal.

2.5.2. Edge detection

Algorithm-1

First, Regularized WCV (RWCV) criterion is calculated for the radial image of angle *i* and accordingly its minimum point is selected as the most obvious border in the image by using equations (4)- (17). Regarding the larger radius of the MA border than the lumen border, as well as the explanations on various types of border brightness textures in the IVUS images provided in section 1, this point is labeled as the MA border named $B_{MA}(i)$ in the global state. In terms of the radial position, the lumen border is located at a smaller radius relative to the MA border. Therefore, at each angle, the function of RWCV criterion is recalculated for the upward part of the MA-labeled point by using equations (4)- (17) and its minimum point is selected as the radial position with the second degree of importance and labeled as the lumen border named $B_L(i)$. The same procedure is done for the radial image of all angles.

Since the proposed algorithm is based on the radial brightness intensity distribution, the algorithm output is sensitive to the presence of the artifacts. Therefore, the border should be corrected while facing such circumstances. The detection and correction of such cases are described in Algorithm 2.

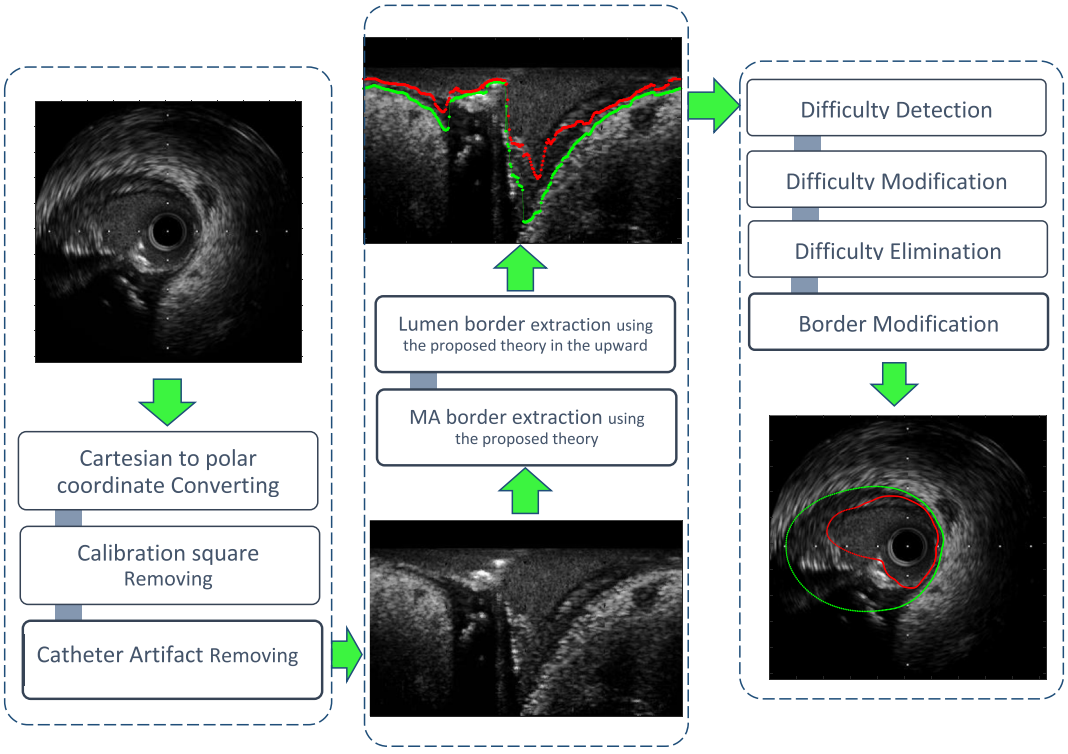

Fig. 2. Flow diagram of the proposed border detection process.

Algorithm-2: Ad-hoc

The main idea of algorithm-2 is based on comparing the variation of two continuous borders obtained from juxtaposing the labeled points. For this purpose, two sets of the points obtained from Algorithm-1 including the lumen border points, B_L, and the MA border points, B_{MA} are used. This algorithm is composed of the following steps:

***1. Difficulty detection*:** First, the MA border is selected as the reference border, and the first-order derivative of this border (equivalent to angle-to-angle difference) is calculated. The derivative is considered as a vector quantity, the variations and sign of which indicate whether it is higher (+sign) or lower (- sign) at the given angle, compared to its previous angle.

For simplicity, it is first assumed that the problem which can be automatically detected is the presence of calcific plaque, which is known as a dense plaque, which causes shadowing. Then, the most distinct border in the image is related to the calcific region at the starting angle of the calcific region, which is close to the lumen border. Therefore, at this angle, the estimated MA border undergoes a sudden change, leading to a derivative with a high value and negative sign. Then, at the end angle of the calcific region, the newly-labeled border approaches the MA border again, which leads to high value and a positive sign of derivative in the estimated MA border at this angle. In order to determine these points, instead of using a constant threshold, the values of the derivative at each angle with the Euclidean distance of the MA border are compared with all the points of the lumen border. To this aim, a circle with the border point as its center and a diameter equal to the derivative value is considered at each angle of the MA border. A variable named "*Difficulties*" is initialized at its index by the

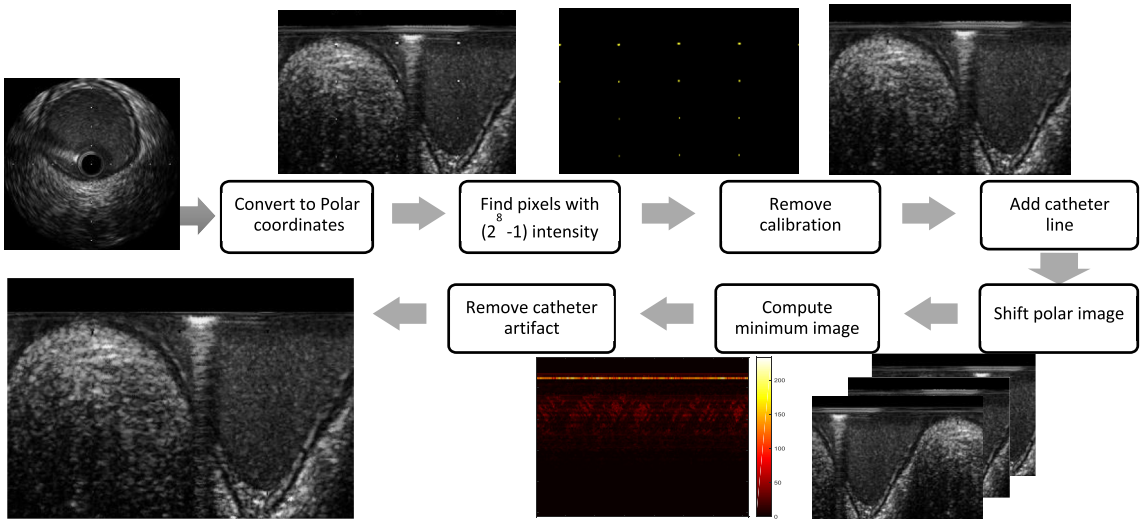

Fig. 3. Preprocessing steps: The removal steps of calibration square artifact as well as estimating the radial position of the catheter artifact and its removal for a sample IVUS Frame.

The Difficulty Detection Algorithm:

1: $B_L \leftarrow$ *Lumen border*
2: $B_{MA} \leftarrow$ *Media-Adventitia Border*
3: $D_{MA} \leftarrow \frac{\partial B_{MA}}{\partial \theta}$
4: **For** *i=1 to number of angle* **do**
5: **For** *j=1 to number of angle* **do**
6: **If** $d^*((i,B_{MA}), (j, B_L)) < \left|\frac{D_{MA}}{2}\right|$
7: *Difficulties(i)* $\leftarrow$ *sign(D_{MA}(i))*
8: *break*
9: **Else**
10: **If j==** *number of angle*
11: *Difficulties(i)* $\leftarrow$ *0*
12: **End if**
13: **End if**
14: **End For**
15: **End For**

* Euclidian distance

Fig. 4. Pseudocode of the difficulty detection step.

number of the circle center and is assigned by the sign of the derivative of the MA border if there is a point of the lumen border within the circle. Otherwise, the value of *Difficulties* at its index by the number of the circle center is equal to zero.

Considering the artificial effect of the guidewire, it is observed that it has the same effect as the dense plaque at the output of Algorithm-1. The above-mentioned method can recognize the presence of the guidewire artifact properly since the most distinct border is close to the catheter in this type of artifact. Fig. 4 displays the pseudocode related to this step.

2. Difficulty Modification: There is no problem if the first and last non-zero values of the *Difficulties* are -1 and $+1$, respectively. However, when the first non-zero value of the variable is $+1$ and its last non-zero value is -1, it means that the calcific region is located at the cutting angle of converting the Cartesian into Polar coordinates. Therefore, in this case, the "*Difficulties*" variable is initialized as -1 for the start angle (0°) and $+1$ for the end angle (359°) in order to create a complete revolution at the border.

When the first non-zero value of the variable is $+1$, but its last non-zero value is not -1, it implies the occurrence of an error in detecting such an angle status. In this case, from the start angle up to the first -1 value, the *Difficulties* will be assigned with 0 until removing all the angles which have been mistakenly selected as the endpoint.

The procedure described in the previous paragraph is performed similarly for the end angles. In other words, when the last non-zero value of the variable is -1, but its first non-zero value is not $+1$, means that a mistake occurs in selecting the end angle as the starting point of the calcific region. In such circumstance, inversely from the last angle up to the first $+1$ value, the "*Difficulties*" is assigned 0 until all the angles which have been mistakenly selected as the endpoints are removed.

The last two procedures have no priority over each other so that their order cannot have any effect on the final result.

3. Difficulty Elimination: The obtained "*Difficulties*" is used to remove the MA and lumen borders at those angles with the starting and ending points specified in this variable. The removal of borders begins at the index of the first -1 value and continues up to the index of the first $+1$ value. This procedure is similarly performed for all -1 and $+1$ pairs in the *Difficulties*. In fact, this procedure leads to the removal of the estimated borders located in the discontinuous region.

4. Border Modification: The piecewise interpolation technique is used to complement the border at the removed angles. Since this process is performed in the polar coordinates, both lumen and MA borders form a closed curve in the Cartesian coordinates, and such a closed curve is converted into a restricted curve in the polar coordinates. In order to maintain the curve closed structure in the Cartesian coordinates, the value of the curve, as well as the values of the first and second derivatives of the border at the start angle should be equal to that of the end angle in the polar coordinates. Hence, the periodic cubic spline method is used to achieve the maximum smoothness at the cutting angle of the conversion from the Cartesian into polar coordinates [33].

$$S(\theta) = \begin{cases} C_1(\theta). & \theta_1 \le \theta \le \theta_2 \\ \quad \cdots & \\ C_i(\theta). & \theta_i \le \theta \le \theta_{i+1} \\ \quad \cdots & \\ C_{n-1}(\theta). & \theta_{n-1} \le \theta \le \theta_n \end{cases} \tag{22}$$

where each $C_i = a_i + b_i\theta + c_i\theta^2 + d_i\theta^3$ is considered as a cubic function, which involves the two following end conditions, in addition to the continuity in the first and second derivatives at the border points:

$$D^1[S(\theta_1)] = D^1[S(\theta_{end})] \tag{23}$$

$$D^2[S(\theta_1)] = D^2[S(\theta_{end})] \tag{24}$$

where $D^r[\ldots]$ represents the rth-order derivative, $S(x)$ is the estimated piecewise polynomial, and θ_1 and θ_{end} indicate the initial and end angles of the polar image, respectively. The applied interpolation features the lowest rate of Runge's phenomenon, compared to the common integrated interpolation methods. By considering all the boundary conditions, the equation is converted into a tridiagonal linear system with a single unique solution [33]. Once the piecewise polynomial is calculated, the lumen border named B^L_{auto} and MA border named B^{MA}_{auto} are extracted for discrete points with 1-degree resolution in the polar coordinates. Then, the moving average is used to obtain a quantitatively smooth border:

$$C^{MA}_{auto}[i] = \frac{1}{M} \times \sum_{j=0}^{M-1} B^{MA}_{auto}[i+j] \tag{25}$$

$$C^{L}_{auto}[i] = \frac{1}{M} \times \sum_{j=0}^{M-1} B^{L}_{auto}[i+j] \tag{26}$$

where M indicates the number of points involved in the averaging process. Regarding the limited lateral resolution in the IVUS imaging [31] and the cut of frequency (f_c) of the moving average filter [34], the optimal value of M is selected equal to 31:

$$M_{opt} = \frac{0.443}{f_c} \times F_s = \frac{0.443}{\frac{r_d}{P_d}} \times 360 = 31 \tag{27}$$

where F_s (frequency sampling) is equal to the number of border points (360), r_d represents the mean of the lateral resolution ($150\mu m$), Pd is considered as pixel resolution mean ($30\mu m$), and $\cdots$ is the notation of the largest integer less than or equal to the variable. Finally, the border points are converted to the Cartesian coordinates. An example of the lumen and MA borders before and after applying Algorithm-2 is shown in Fig. 5.

2.6. Evaluation metrics

Three sets of metrics are used to evaluate the borders obtained by the proposed process. The first set includes three standard metrics, namely Hausdorff distance (HD), Jaccard measure (JM), and percentage of area difference (PAD), which were used in Ref. [6], as well as all the methods utilizing the standard dataset. Selecting these metrics will provide the ground for a fair comparison between the method proposed in the present work and other methods.

HD calculates the maximum distance of the minimum Euclidean

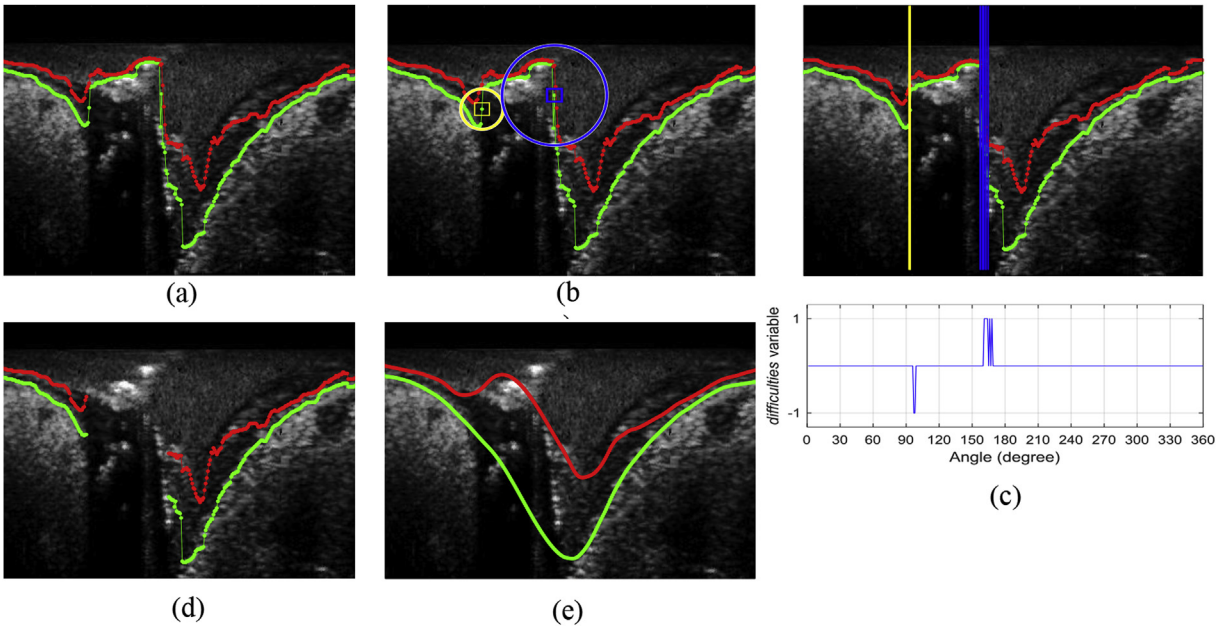

Fig. 5. An example of the points on the lumen(red) and MA(green) borders: (a) before applying algorithm-2, and During step-by-step implementation of algorithm-2: (b) two sample circles along with their corresponding centers that cover the points of the Lumen boundary (blue: positive derivative, yellow: negative derivative), (c) *Difficulties* variable, (d) elimination of the MA and lumen borders located in the discontinuous region, (e) cubic spline interpolation along with the smoothing procedure.

distance between any point on a border and another border [35]:

$$D(C_{auto}.\ C_{man}) = \max_{a \varepsilon C_{auto}} \left(\min_{b \varepsilon C_{man}} a - b \right) \tag{28}$$

where C_{auto} and C_{man} indicate the automatic and manual borders, respectively, and $\|\cdot\|$ is considered as the Euclidean distance. In the present study, the two-sided HD, measured in millimeter, was used as follows [6]:

$$HD(C_{auto}.\ C_{man}) = max\{D(C_{auto}.\ C_{man}).\ D(C_{man}.\ C_{auto})\} \tag{29}$$

JM calculates the ratio of the overlapping area of the automatic and manual borders to the total area of both borders [6]:

$$JM(R_{auto}.\ R_{man}) = \frac{R_{auto} \cap R_{man}}{R_{auto} \cup R_{man}} \tag{30}$$

where R_{auto} and R_{man} indicate the areas shared by the C_{auto} and C_{man} borders. The JM measure value ranges between 0 and 1.

PAD calculates the relative difference between the areas obtained from the automatic (A_{auto}) and manual (A_{man}) borders:

$$PAD(A_{auto}.\ A_{man}) = \frac{|A_{auto} - A_{man}|}{A_{man}} \tag{31}$$

In this research, the PAD value was expressed as a number between 0 and 1.

In addition, the paired *t*-test with a significance level of 0.05 (alpha = 0.05) was conducted in order to compare the method used in the present work with those of other studies which used the joint standard dataset. Since the number of the samples is more than 30 (the sample size of the test set of dataset A and B is 58 and 326, respectively), and the real variance of the population is unknown, the use of the *t*-test is more rational than the other parametric and non-parametric tests although none of the calculated measures has a normal distribution [36]. In addition, the significance level of 0.05 is a feasible level for conducting research work although the lower significance level (e.g. 0.01) has a lower type I and II errors [37].

Regarding the second set, the comparisons were made between the average lumen diameter (ALD) of the automatic border and that of the manual border, as well as between the lumen area (LA) of automatic border and LA of the manual border by involving the latest up-to-date applications of the IVUS imaging for the luminal measurement purposes, especially stenting. Further, the regression analysis was used to compare these two parameters quantitatively. Thus, the ALD is defined as follows:

$$ALD = \frac{1}{N} \sum_{i=1}^{N} 2 \times r_i \tag{32}$$

where N indicates the total number of the points within the border curve and r_i represents the radius of the ith point related to the center of the catheter.

Given the third set, three standard position error measures such as Maximum distance error (MaxD), Mean distance error (MeanD), and Mean signed distance error (MSD) [38], along with the wall thickness measure like wall thickness error (WTE) [39] were used to analyze the clinical aspects of the proposed process.

With respect to position error measures, the distance of each pixel of the automatic border to the closest point on the manual border is calculated as follows [38]:

$$D_{C_{man}}(a) = \min_{b \varepsilon C_{man}} \|a - b\| \tag{33}$$

where a represents the pixel of the automatic border, C_{man} indicates the manual border, and $\|\cdot\|$ is regarded as the Euclidean distance. MaxD calculates the maximum of $D_{C_{man}}$ as follows [38]:

$$MaxD = \max_{a \varepsilon C_{auto}} \left(D_{C_{man}}(a) \right) \tag{34}$$

where C_{auto} indicates the automatic border. In this study, MaxD was measured in millimeter. MeanD calculates the mean of $D_{C_{man}}$ as follows [38]:

$$MeanD = \underset{a \varepsilon C_{auto}}{\text{mean}} \left(D_{C_{man}}(a) \right) \tag{35}$$

In this study, MeanD was measured in millimeter. MSD calculates the signed mean of $D_{C_{man}}$ [38]:

$$MSD = \underset{a \varepsilon C_{auto}}{\text{mean}} (SgnD(a)) \tag{36}$$

where $SgnD(a)$ weights the value $D_{C_{man}}(a)$ depending on whether the pixel a lies inside or outside of the manual border [38]. In this study, MSD was measured in millimeter.

Regarding the wall thickness error, the average wall thickness of each frame was calculated for both automatic and manual borders. Further, the cumulative distribution and regression analysis were used in order to evaluate this measure quantitatively.

3. Results

In this section, the proposed theory is used to evaluate the synthetic images first. In this regard, a qualitative comparison was made between the radial threshold theory and the Otsu's method. Then, the proposed RWCV criterion was compared with the common criteria used in the previous studies, followed by the evaluation of the parameter λ variations. In the next procedure, the proposed border detection process was evaluated both quantitatively and qualitatively. In the quantitative evaluation, the proposed process with/without ad-hoc (Algorithm-2) was self-evaluated and accordingly the obtained results were compared (self-evaluation). The quantitative results are reported in a series of tables. Regarding the self-evaluation, the metrics associated with the stenting applications and the metrics of clinical evaluation (the third set of defined metrics) were investigated separately, along with the standard metrics presented in Ref. [6] In addition, the sensitivity analysis of the proposed process was reported. Further, the proposed method was compared with the previous methods which used the standard data during recent years via the statistical t-test (comparative evaluation). Regarding the qualitative evaluation, two sets of images are shown to analyze faster and easier. First, out of each available dataset, a sample image with no artifact-no plaque, no artifact-with plaque, bifurcation, stent, side vessel, shadow, guidewire artifact, and catheter one vessel wall categories, are shown along with the borders obtained from the automatic method, as well as the borders extracted by an expert. Second, out of each dataset for each border are displayed by three images with the worst, moderate, and best border extraction results, respectively.

3.1. Evaluation of radial threshold theory

The first row in Fig. 6 illustrates the result of implementing the proposed radial threshold search theory in a synthetic image (Fig. 6(a)) with three ranges of speckle noise. In addition, the results of the Otsu's [20] method for the same image were provided in the second row of the same figure. Although the proposed theory aimed to estimate the radius as threshold, the Otsu's method sought to estimate the brightness intensity as the threshold. However, based on a qualitative comparison made between the results provided in two rows of the figure, it is obvious that segmentation through radial threshold method is closer to the ground truth image, compared with the segmentation by the Otsu's method.

In order to determine the effect of the weight parameter λ, the radial threshold theory was investigated by the RWCV criterion for $\lambda\varepsilon(0.1]$ on a synthetic image with PSNR = 11.5 dB by using the JM. Fig. 7(b) represents the JM for λ variations. λ = 0.5 was selected for the purpose of the present study since this metric displays minimum variations in the range of (0.1–0.95) for λ values.

Subsequently, the proposed radial threshold theory was evaluated in terms of the proposed RWCV criterion (λ = 0.5), the common WCV criterion [20], and the modified WCV criterion presented in Ref. [27] (WCV plus discrepancy factor). To this aim, the radial threshold method was performed with each criterion in a wide range of the input image PSNRs, and the JM of the segmented image was calculated compared to the ground truth image. Fig. 7(c) displays the variation of JM related to the PSNR image for each criterion. Three major points can be inferred from this diagram. First, the proposed criterion yields higher JM values for low PSNRs. Second, the proposed RWCV criterion is more robust in case of PSNR variations. Finally, the proposed theory is highly stable for PSNR greater than 13 dB. Fig. 7(d) illustrated each of the criteria for a sample radial image depicted in Fig. 7(a). In addition, Fig. 8 displays the receiver operating characteristic (ROC) of the proposed RWCV along with ROC of the common criteria used in the previous studies. As shown, the area under ROC (AUC) was involved. Regarding the ROCs and AUCs, it is concluded that the proposed algorithm has a high accuracy (no matter what type of criterion is used), and the proposed RWCV criterion improves the overall AUC value by 0.05.

3.2. Quantitative analysis of border detection process

3.2.1. Quantitative self-evaluation

In this section, a self-evaluation was performed on the proposed method with/without ad-hoc using JM, HD, and PAD in order to prove the capability of the proposed method to extract the lumen and MA borders, as well as proving the effectiveness of the ad-hoc (Algorithm-2). Based on this evaluation, the contours obtained from the automatic method were compared with the mean of two manual contours. Tables 2 and 3 represent the performance of the proposed process with/without the ad-hoc algorithm, along with intra- and inter-observer evaluations for each individual category, and the general performance

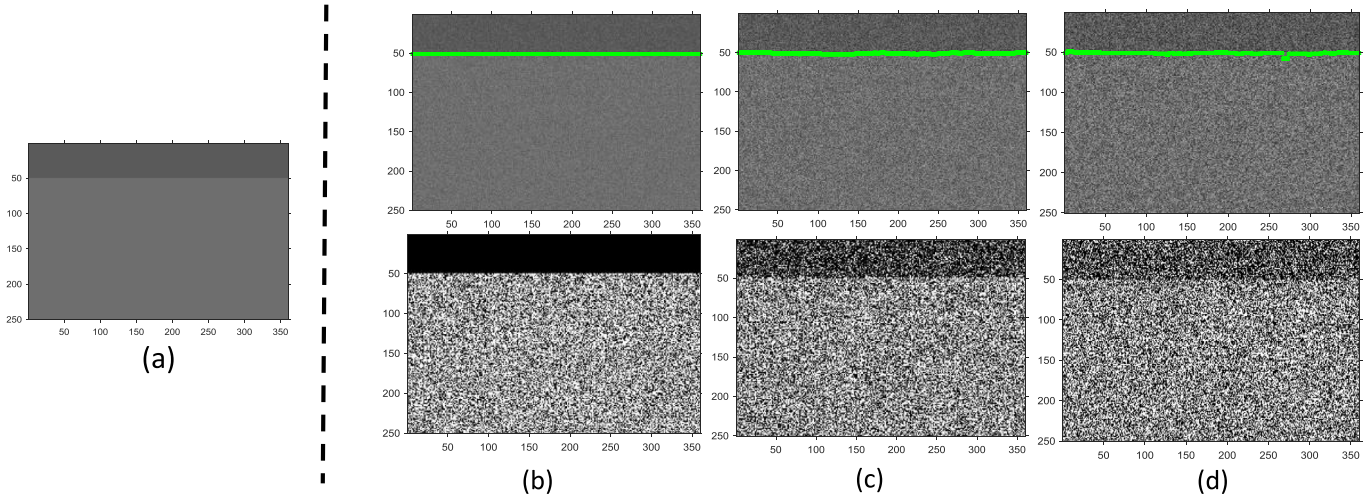

Fig. 6. (a) A sample synthesis image, and the result of implementing the proposed radial threshold theory (green lines in first row) and the Otsu's method (second row) for three PSNR, (b) PSNR = 26 dB, (c) PSNR = 20 dB, (d) PSNR = 17 dB.

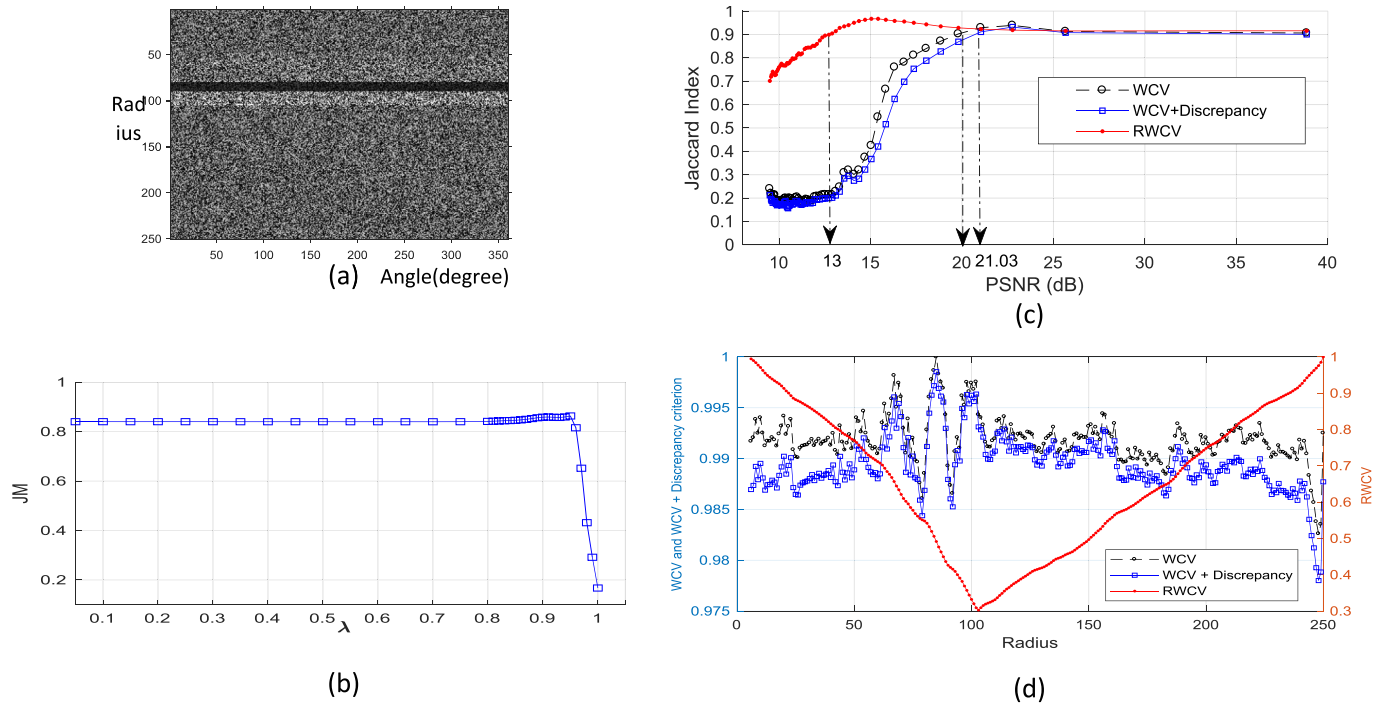

Fig. 7. (a) Sample synthesis image, (b) JM metric variations for λ variations, (c) JM metric variations related to the image PSNR for three criteria: RWCV (the proposed criterion), WCV [20], and WCV with discrepancy factor [27], (d) RWCV, WCV, and WCV with discrepancy factor for Angle = 100° in (c).

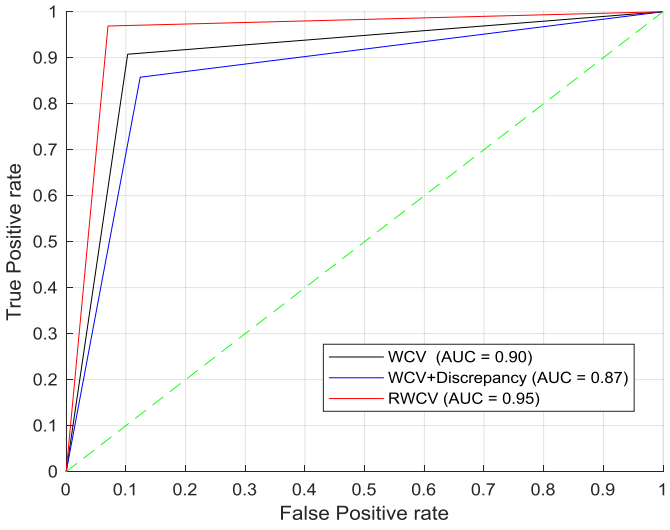

Fig. 8. ROC curves of the proposed method for RWCV (the proposed criterion), WCV [20], and WCV with discrepancy factor [27] (The AUCs are included in the legend).

of the proposed algorithm with/without ad-hoc for Dataset A and B, respectively. The evaluation of the proposed method indicated that both metrics yield reliable results, compared to the intra- and inter-observer evaluations. In addition, the proposed method could exhibit higher accuracy for dataset B than dataset A regarding the general performance.

Regarding the general performance of the proposed process, the ad-hoc algorithm yielded the mean improvement of 0.10, 0.89 mm, and 0.13 in JM, HD, and PAD, respectively, for the MA border, and the mean improvement of 0.09, 0.16 mm, and 0.22 in JM, HD, and PAD, respectively, for the lumen border, compared to the process without the ad-hoc algorithm in case of applying dataset A. Further, the general performance of the proposed process with the ad-hoc led to the mean improvement of 0.03, 0.34 mm, and 0.08 in JM, HD, and PAD, respectively, for the MA border, and mean improvement of 0.07, 0.20 mm, and 0.21 in JM, HD, and PAD, respectively, for the lumen border, compared with the process without the ad-hoc in case of dataset B. In general, the improvement was seemingly less in dataset B, which can be related to the higher precision of the initial border extraction in this dataset. Furthermore, the highest improvement rate in dataset A was achieved at the MA border for the non-artifact category (i.e. mean improvement of 0.21, 0.77 mm, and 0.41 for JM, HD, and PAD, respectively). Regarding dataset B, the highest improvement rate was obtained for the MA border and the side vessel category with the mean improvement of 0.06, 0.53 mm, and 0.23 for JM, HD, and PAD, respectively.

Fig. 9 displays the linear regression of the ALD for the automatic method, compared to the manual method, and the linear regression of two manual borders obtained by two independent experts. In addition, Fig. 10 illustrates the linear regression of the LA for the automatic method compared to the manual method, and the linear regression of two manual areas obtained by two independent experts. As observed in Figs. 9 and 10, the linear regression analysis of the ALD and LA a very high correlation was reported between the automatic and manual segmentation of the lumen border in dataset B and high correlation between automatic and manual segmentation of the lumen border in dataset A.

Table 4 presents the position error measurement of the lumen and MA borders, along with measuring the wall thickness error. Compared to the intra- and inter-observer evaluations in case of applying dataset A, the absolute position error of the proposed process yielded the mean absolute position error of less than 0.28 mm for the lumen border, and the mean absolute position error of less than 0.5 mm for the MA border. Further, the absolute position error of the proposed process yielded the mean absolute position error of less than 0.05 mm for the lumen border, and the mean absolute position error of less than 0.17 mm for the MA border, compared to the intra- and inter-observer evaluations in case of applying dataset B. In general, the MeanD was less in dataset B, due to the lower resolution of the vessel walls in this dataset. Furthermore, MSD of the proposed process is superior to inter-observer evaluation for the lumen and MA borders in case of applying both datasets A and B. In

Table 2
Performance of the proposed process with/without the ad-hoc (algorithm-2), along with intra- and inter-observer evaluations for each individual category and the general performance of the proposed process for dataset A. The bold texts represent the final results of the proposed process.

		Lumen A			Media A		
		JM	HD	PAD	JM	HD	PAD
General performance	Alg1[a]	0.68 (0.11)	1.62 (0.76)	0.38 (0.24)	0.65 (0.11)	2.21 (0.88)	0.25 (0.18)
	Alg1 + Alg2[b]	**0.77 (0.13)**	**1.46 (1.23)**	**0.16 (0.15)**	**0.75 (0.13)**	**1.32 (0.99)**	**0.12 (0.12)**
	Intra-Obs[c]	0.86(0.10)	1.04(0.95)	0.10(0.10)	0.87(0.11)	1.14(1.00)	0.11(0.14)
	Inter-Obs[d]	0.92(0.06)	0.67(0.52)	0.05(0.06)	0.91(0.07)	0.85(0.60)	0.06(0.07)
No Artifact	Alg1	0.63 (0.14)	1.60 (0.62)	0.66 (0.45)	0.69 (0.10)	1.47 (0.74)	0.47(0.23)
	Alg1 + Alg2	**0.78 (0.13)**	**0.97 (0.42)**	**0.22 (0.31)**	**0.90 (0.04)**	**0.70 (0.30)**	**0.06 (0.03)**
	Intra-Obs	0.95(0.02)	0.30(0.13)	0.00(0.00)	0.96(0.01)	0.24(0.04)	0.01(0.01)
	Inter-Obs	0.92(0.06)	0.61(0.51)	0.05(0.06)	0.94(0.02)	0.34(0.01)	0.03(0.01)
Plaque	Alg1	0.67 (0.10)	1.62 (0.67)	0.41 (0.27)	0.65 (0.11)	2.23 (0.88)	0.25 (0.17)
	Alg1 + Alg2	**0.77 (0.12)**	**1.44 (1.14)**	**0.15 (0.13)**	**0.75 (0.13)**	**1.33 (0.97)**	**0.12 (0.12)**
	Intra-Obs	0.86(0.10)	1.04(0.91)	0.10(0.10)	0.87(0.11)	1.09(0.97)	0.11(0.14)
	Inter-Obs	0.92(0.05)	0.65(0.51)	0.04(0.05)	0.91(0.07)	0.86(0.62)	0.07(0.08)
Bifurcation	Alg1	0.68 (0.14)	1.97 (1.30)	0.23 (0.29)	0.64 (0.11)	2.47 (0.86)	0.22 (0.13)
	Alg1 + Alg2	**0.64 (0.14)**	**2.76 (1.67)**	**0.26 (0.17)**	**0.72 (0.14)**	**1.49 (1.13)**	**0.15 (0.17)**
	Intra-Obs	0.88 (0.08)	0.88(0.80)	0.05(0.04)	0.86(0.12)	1.34 (1.31)	0.11(0.12)
	Inter-Obs	0.91 (0.05)	0.73(0.64)	0.05(0.05)	0.89(0.06)	1.08 (0.62)	0.08(0.07)
Stent	Alg1	0.71 (0.08)	1.49 (0.53)	0.34 (0.19)	0.68 (0.10)	1.94 (0.67)	0.22 (0.16)
	Alg1 + Alg2	**0.80 (0.11)**	**1.31 (1.08)**	**0.14 (0.12)**	**0.71 (0.14)**	**0.96 (0.79)**	**0.12 (0.15)**
	Intra-Obs	0.86(0.09)	1.02(0.75)	0.07(0.08)	0.86(0.11)	1.06(0.75)	0.13(0.15)
	Inter-Obs	0.91(0.08)	0.71(0.65)	0.05(0.08)	0.91(0.06)	0.79(0.57)	0.07(0.07)
Side Vessels	Alg1	0.66 (0.09)	1.56 (0.51)	0.49 (0.23)	0.66 (0.10)	2.16 (0.99)	0.27 (0.22)
	Alg1 + Alg2	**0.80 (0.06)**	**0.98 (0.38)**	**0.10 (0.09)**	**0.81 (0.11)**	**1.52 (1.12)**	**0.14 (0.14)**
	Intra-Obs	0.82(0.09)	1.22(0.75)	0.14(0.10)	0.86(0.11)	1.27(0.90)	0.12(0.16)
	Inter-Obs	0.92(0.06)	0.55(0.40)	0.04(0.05)	0.89(0.10)	1.05(0.84)	0.10(0.11)
Shadow artifact	Alg1	0.68 (0.11)	1.54 (0.67)	0.40 (0.27)	0.63 (0.11)	2.38 (0.94)	0.20 (0.13)
	Alg1 + Alg2	**0.77 (0.12)**	**1.40 (1.08)**	**0.15 (0.13)**	**0.72 (0.13)**	**1.51 (1.08)**	**0.14 (0.14)**
	Intra-Obs	0.85(0.09)	1.03(0.88)	0.10(0.09)	0.89(0.08)	1.06(0.92)	0.07(0.07)
	Inter-Obs	0.91(0.05)	0.70(0.55)	0.05(0.06)	0.92(0.07)	0.79(0.64)	0.06(0.07)
Guidewire artifact	Alg1	0.65 (0.11)	1.94 (0.86)	0.39 (0.30)	0.65 (0.12)	2.45 (1.01)	0.23 (0.13)
	Alg1 + Alg2	**0.73 (0.14)**	**1.83 (1.46)**	**0.17 (0.14)**	**0.73 (0.13)**	**1.60 (1.11)**	**0.13 (0.11)**
	Intra-Obs	0.88(0.08)	0.92(0.81)	0.08(0.09)	0.87(0.10)	1.08(0.96)	0.13(0.16)
	Inter-Obs	0.93(0.05)	0.56(0.44)	0.04(0.06)	0.91(0.06)	0.78(0.57)	0.07(0.08)
Catheter 1 vessel wall	Alg1	0.69 (0.11)	1.44 (0.55)	0.38 (0.28)	0.63 (0.11)	2.30 (0.80)	0.25 (0.20)
	Alg1 + Alg2	**0.77 (0.11)**	**1.30 (0.95)**	**0.14 (0.12)**	**0.75 (0.13)**	**1.19 (0.84)**	**0.11 (0.11)**
	Intra-Obs	0.86(0.11)	0.99(1.01)	0.10(0.12)	0.86(0.13)	1.17(1.05)	0.12(0.17)
	Inter-Obs	0.92(0.06)	0.59(0.44)	0.04(0.06)	0.92(0.07)	0.80(0.56)	0.06(0.08)

[a] Algorithm-1.
[b] Algorithm-2(ad-hoc).
[c] Intra-observer.
[d] Inter-observer.

addition, Fig. 11 demonstrates the cumulative distribution of the absolute and signed WTE between the proposed method and manual borders, along with evaluating the intra- and inter-observer. Regarding the absolute wall thickness error of the proposed process compared to the intra- and inter-observer evaluations, the mean WTE difference is less than 0.37 mm and 0.13 mm for applying dataset A and B, respectively.

In order to evaluate the clinical relevance of the proposed algorithm, the wall thickness and vessel wall volume were estimated throughout the spatial distribution of the coronary artery. The clinical evaluation was performed on the test set of this dataset since the dataset B consisted of 10 distinct patients (2 patients in the train set, and 8 patients in the test set), in which each patient has a series of 20–50 ECG gated frames. The length of the examined vessels ranges between 1.5 and 2.5 cm due to the pullback speed of 0.5 mm/s. In order to show the reliability of the algorithm during a pullback, the average wall thickness during a pullback, and the vessel wall volume of a pullback were implemented. Fig. 12 displays two critical results of 8 patients in the test set of dataset B which had maximum wall thickness error, along with artery borders obtained by the proposed method and the manual segmentation delineated by experts by considering the average wall thickness during a pullback. Red and green color curves are related the lumen and MA borders, respectively. However, dashed and solid curves indicate the borders of the proposed method and manual segmentations, respectively. The longitudinal image indicates the cut-plane of 150^0. In addition, the vessel wall volume of the pullbacks obtained by the proposed method was calculated, along with the manual segmentation. Further, the regression analysis was used to compare quantitatively. As illustrated in Fig. 13, the automatic detection of stenosis, which is very important from a clinical point of view, is possible by considering the low error values of the average wall thickness of the proposed process compared to the manual segmentations, as well as the high correlation of the vessel wall volume between the proposed process and manual segmentations.

In order to evaluate the reliability of the proposed method, the ROC curve is demonstrated in Fig. 14. Furthermore, the intra- and inter-observer ROCs are plotted. As shown, the AUCs are included.

The One-at-a-time (OAT) [40] method was used to analyze the sensitivity of the proposed process. In this method, a variable is changed while other variables are fixed during an experiment [40]. The proposed three-step process includes angle resolution of the radial images as the main variable. namely search zone box. Regarding the search zone box, the proposed three-step process was repeated for five dimensions of the search zone box including 1 (the proposed search zone box), 5, 10, 15, and 20°, along with WTE was calculated for both datasets A and B. Fig. 15 and Table 5 represent the results. Narrower search zone box leads to less wall thickness error. The proposed search zone box could yield the mean WTE improvement of 0.13 mm and

Table 3
Performance of the proposed process with/without the ad-hoc (algorithm-2), along with intra- and inter-observer evaluations for each individual category, and the general performance of the proposed process for dataset B. The bold texts represent the final results of the proposed process.

		Lumen B			Media B		
		JM	HD	PAD	JM	HD	PAD
General performance	Alg1[a]	0.77 (0.09)	0.58 (0.28)	0.31 (0.17)	0.79 (0.11)	0.98 (0.56)	0.21 (0.28)
	Alg1 + Alg2[b]	**0.84 (0.07)**	**0.38 (0.26)**	**0.10 (0.08)**	**0.82 (0.11)**	**0.64 (0.41)**	**0.13 (0.11)**
	Intra-Obs[c]	0.88(0.05)	0.28(0.13)	0.11(0.08)	0.92(0.03)	0.24(0.12)	0.06(0.04)
	Inter-Obs[d]	0.93(0.05)	0.17(0.13)	0.04(0.06)	0.95(0.03)	0.14(0.10)	0.03(0.03)
No Artifact	Alg1	0.75 (0.08)	0.66 (0.23)	0.35 (0.15)	0.85 (0.06)	0.66 (0.27)	0.11 (0.09)
	Alg1 + Alg2	**0.85 (0.07)**	**0.36 (0.21)**	**0.10 (0.08)**	**0.87 (0.05)**	**0.43 (0.23)**	**0.11 (0.06)**
	Intra-Obs	0.88 (0.05)	0.28 (0.13)	0.11 (0.08)	0.92 (0.03)	0.24 (0.12)	0.06 (0.04)
	Inter-Obs	0.93 (0.05)	0.17 (0.13)	0.04 (0.06)	0.95 (0.03)	0.14 (0.12)	0.03 (0.03)
Plaque	Alg1	0.77 (0.09)	0.58 (0.28)	0.31 (0.17)	0.79 (0.11)	0.98 (0.56)	0.21 (0.28)
	Alg1 + Alg2	**0.85 (0.07)**	**0.38 (0.26)**	**0.11 (0.08)**	**0.82 (0.10)**	**0.64 (0.41)**	**0.13 (0.11)**
	Intra-Obs	0.88(0.05)	0.28(0.13)	0.11(0.08)	0.92(0.03)	0.24(0.12)	0.06(0.04)
	Inter-Obs	0.93(0.05)	0.17(0.13)	0.04(0.06)	0.95(0.03)	0.14(0.10)	0.03(0.03)
Bifurcation	Alg1	0.71 (0.10)	0.77 (0.30)	0.40 (0.22)	0.70 (0.12)	1.50 (0.56)	0.39 (0.38)
	Alg1 + Alg2	**0.83 (0.07)**	**0.47 (0.32)**	**0.12 (0.08)**	**0.74 (0.13)**	**0.99 (0.53)**	**0.22 (0.20)**
	Intra-Obs	0.88 (0.04)	0.30 (0.12)	0.09 (0.06)	0.92 (0.02)	0.24 (0.09)	0.06 (0.03)
	Inter-Obs	0.92 (0.07)	0.18 (0.21)	0.05 (0.09)	0.95 (0.04)	0.15 (0.13)	0.03 (0.03)
Side Vessels	Alg1	0.83 (0.07)	0.41 (0.26)	0.21 (0.12)	0.71 (0.12)	1.30 (0.66)	0.39 (0.38)
	Alg1 + Alg2	**0.85 (0.08)**	**0.34 (0.32)**	**0.11 (0.09)**	**0.77 (0.12)**	**0.77 (0.46)**	**0.16 (0.13)**
	Intra-Obs	0.88 (0.05)	0.30 (0.13)	0.10 (0.08)	0.92 (0.04)	0.24 (0.11)	0.06 (0.04)
	Inter-Obs	0.91 (0.05)	0.20 (0.11)	0.06 (0.05)	0.95 (0.03)	0.15 (0.10)	0.03 (0.04)
Shadow artifact	Alg1	0.82 (0.08)	0.44 (0.31)	0.22 (0.13)	0.68 (0.11)	1.42 (0.48)	0.33 (0.38)
	Alg1 + Alg2	**0.83 (0.07)**	**0.36 (0.22)**	**0.11 (0.07)**	**0.72 (0.12)**	**1.01 (0.39)**	**0.12 (0.13)**
	Intra-Obs	0.88 (0.05)	0.31 (0.13)	0.11 (0.08)	0.92 (0.04)	0.27 (0.15)	0.06 (0.05)
	Inter-Obs	0.93 (0.05)	0.18 (0.14)	0.04 (0.06)	0.96 (0.03)	0.14 (0.10)	0.02 (0.02)

[a] Algorithm-1.
[b] Algorithm-2(ad-hoc).
[c] Intra-Observer.
[d] Inter-Observer.

0.28 mm for dataset A and B, respectively, compared to the largest search zone box of the OAT experiment.

3.2.2. Comparative quantitative analysis

In this regard, the general performance of the proposed method was compared with all the recent studies, which evaluated their methods by using the dataset [6] (Table 6). The empty row in the table means that the researchers did not implement their method for that specific category of data. Paired sample *t*-test at the significance level of 5% is used to show whether the metric difference between the proposed method and state-of-the-art is significantly different or not. As shown in Table 7, the order of comparing the metrics is JM, HD, and PAD. In this table,

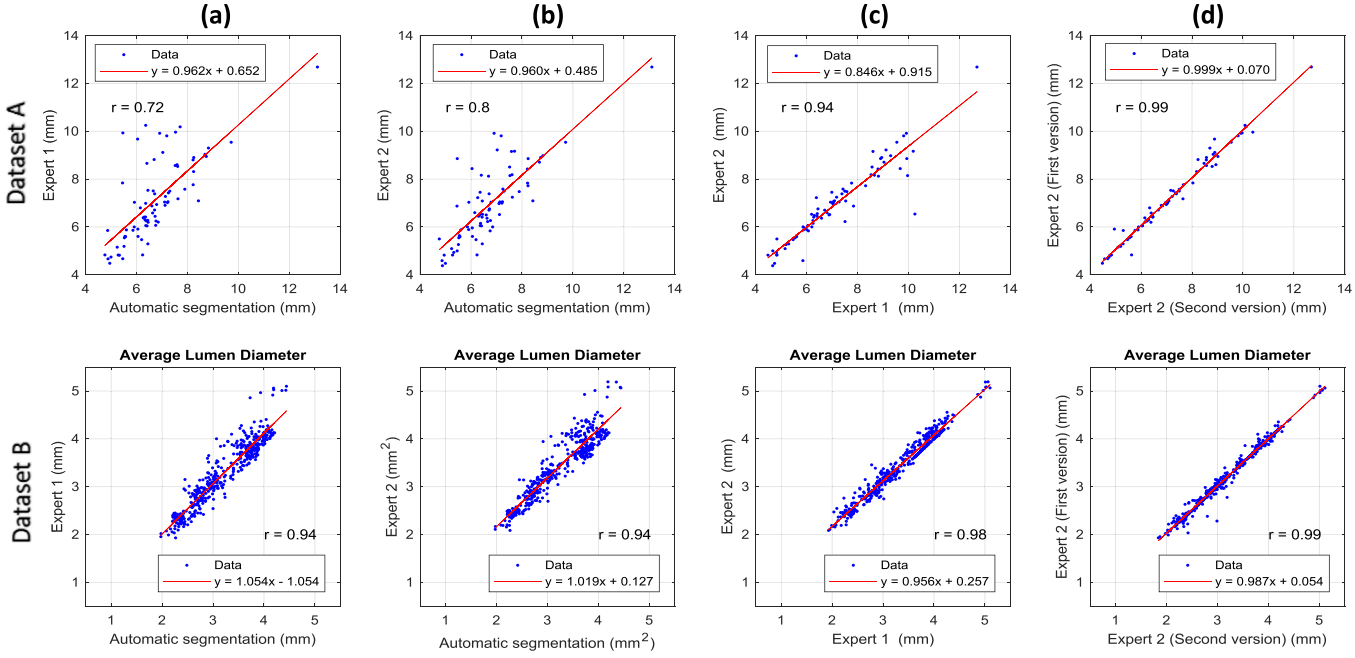

Fig. 9. (a and b) Linear regression of the ALD in the borders obtained by the proposed method in comparison to ALD in two manual borders obtained by two experts, (c) linear regression of the ALD of two manual borders obtained by two independent experts, (d) linear regression of the ALD of two manual borders obtained by an expert over a discontinuous interval (The first and second rows are related to dataset A B, respectively).

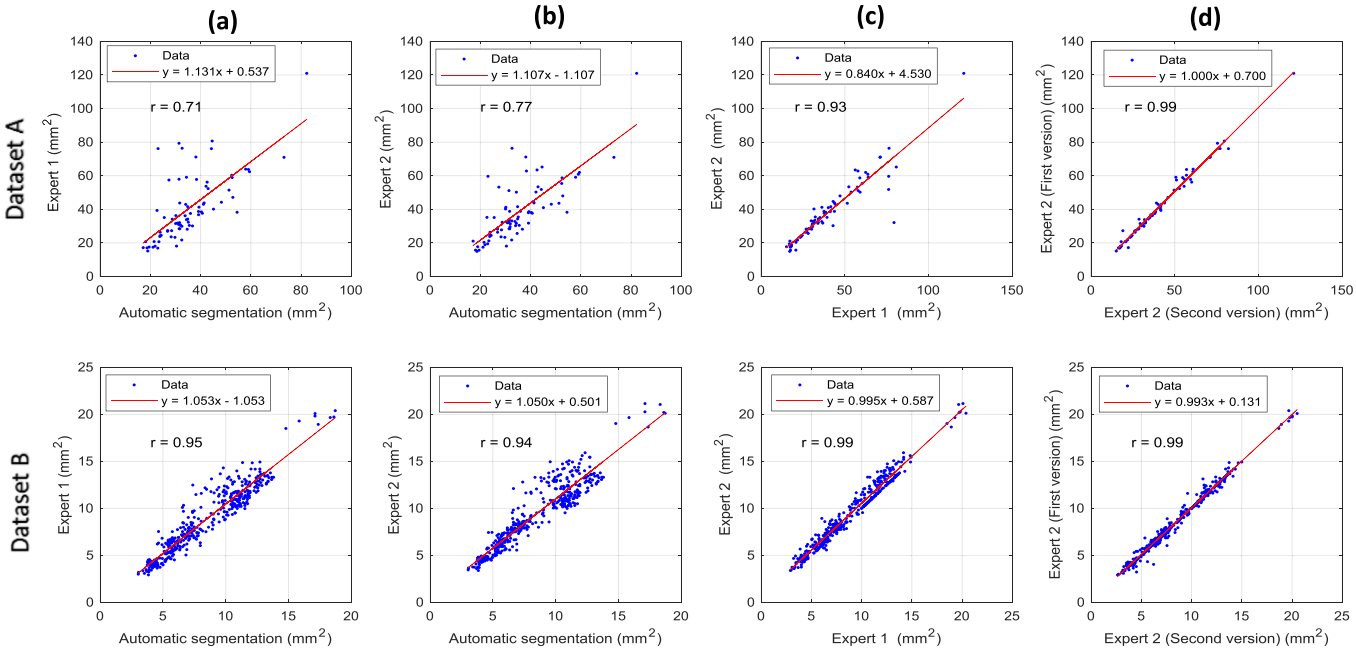

Fig. 10. (a and b) Linear regression of the LA of the borders obtained by the proposed method in comparison to LA of two manual borders obtained by two experts, (c) linear regression of the LA of two manual borders obtained by two independent experts, (d) linear regression of the LA of two manual borders obtained by an expert over a discontinuous interval (The first and second rows are related to dataset A B, respectively).

the "+" sign for each metric indicates the distinction and superiority of the proposed method to the one in the intended previous study, while the "-" sign for each metric represents the distinction and weakness of the proposed method, compared to the method used in the previous work. In addition, the "N" sign for each metric means that there is no significant difference between the two methods. The empty column means that the previous study failed to provide any results for this category.

3.3. Qualitative analysis of border detection process

Fig. 16(a) and (b)display the frames with the various categories for dataset A and dataset B, respectively. Since dataset B lacks the stent, guidewire artifact, and catheter one vessel wall artifact, their corresponding positions in Fig. 16 (b) were remained empty. As illustrated, the lumen and MA borders obtained from the proposed process are shown with the continuous red and green curve, respectively. Further, the lumen and MA borders which were obtained manually (first expert of [6]) are shown with red and green dashed curves, respectively.

Regarding a large number of frames in the datasets, three types of results including *worst*, *moderate*, and *best* were provided for dataset A and B in the first and second rows of Fig. 17, respectively, in order to achieve a further intuitive understanding of the extracted borders. In this regard, JM was used for ranking the results obtained for borders, although other metrics led to the same result. Furthermore, the visual evaluation indicates the success of the proposed method in detecting the lumen and MA borders.

4. Discussion

The present study included two main parts. First, a border estimation theory was presented on the radial profile to investigate whether it can detect the borders in the synthetic images similar to the IVUS images. The mean value of 0.92 for JM obtained for a wide range of PSNRs in the IVUS-like synthetic images confirmed the possibility of the border detection by using the proposed theory for the images similar to the structure of the IVUS images.

The qualitative comparison (Fig. 6) related to the border estimation results for the synthetic image, which is close to the structure of the IVUS image, indicated the superiority of the proposed method over the Otsu's method. In addition, this theory is considered as the first step in the radial border search (a border search on the radial profile) in the image, which features the capability to implement the parallel processing independently for each angle. Further, in order to increase the flexibility and stability of the proposed theory, the WCV criterion was regularized by using the differential variance term. As illustrated in Fig. 7, an increase of above 7 dB in the dynamic range and improvement of above 0.05 in the AUC of the algorithm could exhibit the

Table 4
The position error measurement of the lumen and MA borders, along with the wall thickness error measurement.

	Metric	Dataset A			Dataset B		
		Proposed Method	Inter-Obs	Intra-Obs	Proposed Method	Inter-Obs	Intra-Obs
Lumen Border	MaxD	**1.33(0.95)**	0.83(0.63)	0.56(0.40)	**0.37(0.26)**	0.27(0.13)	0.16(0.12)
	MeanD	**0.42(0.26)**	0.22(0.16)	0.14(0.10)	**0.12(0.07)**	0.1(0.04)	0.05(0.03)
	MSD	**0.01(0.33)**	−0.04 (0.20)	0.04 (0.11)	**−0.03 (0.11)**	0.07 (0.05)	0.01 (0.04)
MA Border	MaxD	**1.78(1.07)**	1.00(0.81)	0.76(0.52)	**0.64(0.41)**	0.22(0.12)	0.14(0.10)
	MeanD	**0.70(0.46)**	0.33(0.30)	0.20(0.16)	**0.22(0.13)**	0.08(0.04)	0.05(0.03)
	MSD	**−0.16 (0.64)**	0.12 (0.30)	0.00 (0.19)	**0.08 (0.15)**	0.04 (0.05)	0.01 (0.04)
Wall thickness	WTE	**0.51(0.45)**	0.28(0.24)	0.14(0.14)	**0.16(0.13)**	0.07(0.06)	0.03(0.03)

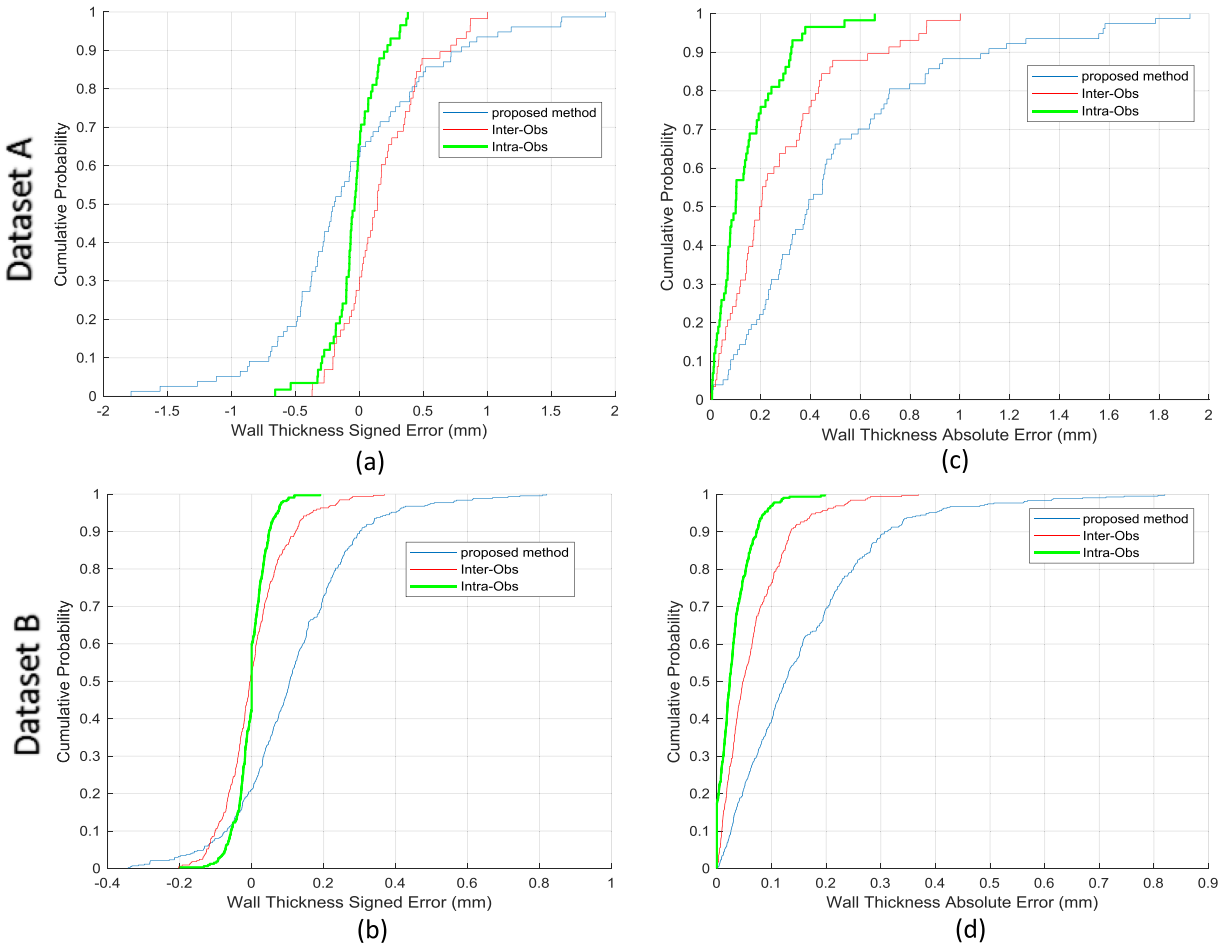

Fig. 11. Cumulative distribution of the Wall Thickness Absolute (c and d) and Signed Errors between the proposed method and manual borders (a and b) (blue curves), along with inter- (red curves) and intra-observer (green curves) variabilities (a and c are related to dataset A while (b and d) are related to dataset B.

outstanding superiority of the proposed criterion to the common WCV criterion. The mean value of 0.92 for JM obtained for a wide range of PSNRs in the IVUS-like synthetic image confirms the possibility of the border estimation by using the proposed theory in the images with the speckle noise similar to the structure of the IVUS images.

Second, a sequential three-step process was suggested based on the radial threshold theory to extract the lumen and MA borders. The first step dealt with preprocessing in order to eliminate the effects of catheter artifact and calibration square artifact. Notwithstanding the identical basics, this step features two major advantages compared with the preprocessing method presented in Refs. [16,17]. First, the removal of the catheter artifact is accomplished through a single frame. Second, unlike the methods proposed in Refs. [16,17], the algorithm cannot lead to a false positive in the case of an input frame with no artifact. In this study, despite the presence of no catheter artifacts in dataset B, dataset A contained the catheter artifact. In the next step, the

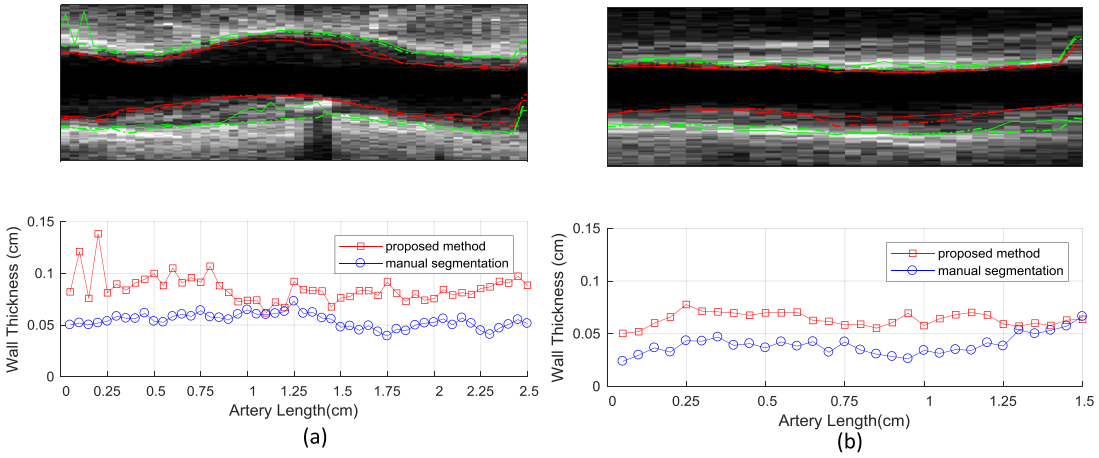

Fig. 12. The average wall thickness (the second row), along with the artery borders obtained by the proposed method and the manual segmentation delineated by experts (the first row): (a) patient #9, (b) patient #10 (Red and green color curves belong to the lumen and Media-Adventitia (MA) borders, respectively).

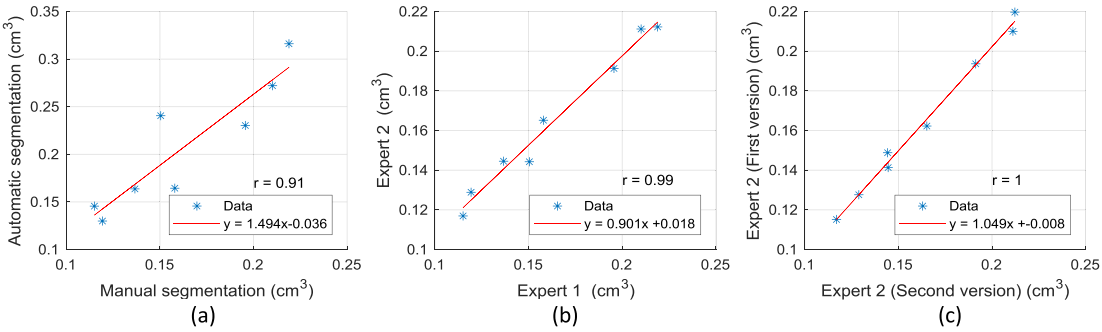

Fig. 13. (a) Linear regression of the vessel wall volume obtained by the proposed method in comparison to the volumes obtained manually, (b) linear regression of the vessel wall volume obtained by two independent experts, (c) linear regression of the vessel wall volume obtained by an expert over a discontinuous interval.

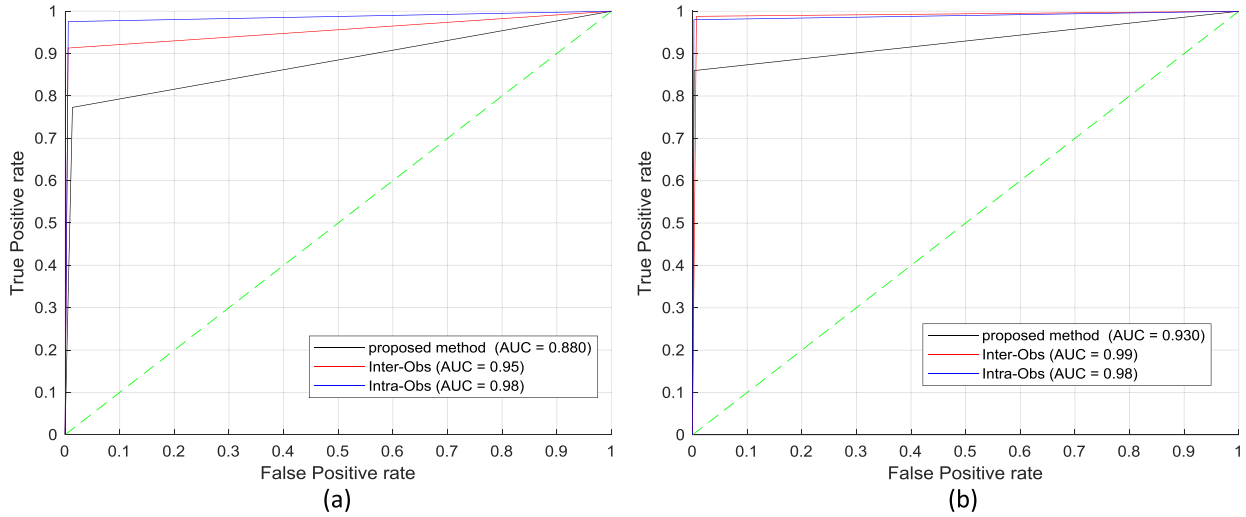

Fig. 14. ROC curves of the proposed process, along with intra- and inter-observer variabilities in dataset A (a), and dataset B (b) (The AUCs are included in the legends).

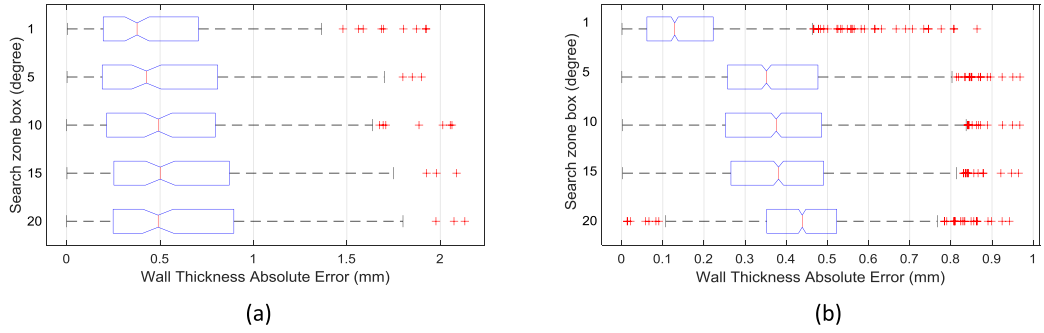

Fig. 15. The wall thickness absolute error of the proposed process for five search zone box dimensions in dataset A (a), and dataset B (b).

Table 5
WTE for five dimensions of the search zone box in 1 (the proposed search zone box), 5, 10, 15, and 20 degrees

Search zone box (degree)	Dataset A					Dataset B				
	20	15	10	5	1[a]	20	15	10	5	1[a]
WTE (mm)	0.64(0.51)	0.63(0.49)	0.61(0.50)	0.58(0.48)	0.51(0.45)	0.44(0.15)	0.38(0.19)	0.37(0.18)	0.35(0.19)	0.16(0.13)

[a] Proposed Method.

estimation process of the lumen and MA borders was presented. Finally, an ad-hoc algorithm was proposed to refine the final borders.

Regarding all the three metrics such as PAD, JM, and HD (Tables 2 and 3), the proposed ad-hoc algorithm yielded positive results for all categories, except for the bifurcation category in the 40 MHz frames (dataset A). Thus, the entire proposed process proves to have high accuracy for the IVUS frames without artifact (with/without plaques) for the lumen and MA border detection in both datasets A and B. Regarding

Table 6
General performance of the proposed method compared with all the recent studies which have evaluated their methods using the standard dataset [6].

	Lumen A			Lumen B			Media A			Media B		
	JM	HD	PAD	JM	HD	PAD	JM	HD	PAD	JM	HD	PAD
Proposed Method	**0.77 (0.13)**	**1.46 (1.23)**	**0.16 (0.15)**	**0.84 (0.07)**	**0.38 (0.26)**	**0.11 (0.08)**	**0.75 (0.13)**	**1.32 (0.99)**	**0.12 (0.12)**	**0.82 (0.11)**	**0.64 (0.41)**	**0.13 (0.11)**
Faraji et al. [16]				0.87 (0.06)	0.30 (0.20)	0.08 (0.09)				0.77 (0.17)	0.67 (0.54)	0.19 (0.18)
Essa et al. [15]							0.84 (0.10)	1.22 (0.72)	0.13 (0.15)			
Jodas et al. [11]				0.88 (0.06)	0.29 (0.17)	0.09 (0.07)						
Wang et al. [6]	0.75 (0.11)	1.78 (1.13)	0.19 (0.12)	0.83 (0.08)	0.51 (0.25)	0.14 (0.12)						
Destrempes et al. [6,14]	0.85 (0.12)	1.16 (1.12)	0.10 (0.12)	0.88 (0.05)	0.34 (0.14)	0.06 (0.05)	0.86 (0.11)	1.18 (1.02)	0.10 (0.11)	0.91 (0.04)	0.31 (0.12)	0.05 (0.04)
Alberti et al. [6]	0.72 (0.12)	1.70 (1.09)	0.22 (0.14)	0.79 (0.08)	0.46 (0.30)	0.16 (0.09)						
Exarchos et al. [6]	0.80 (0.14)	1.32 (1.18)	0.11 (0.12)	0.81 (0.09)	0.42 (0.22)	0.11 (0.11)	0.80 (0.13)	1.57 (1.03)	0.14 (0.16)	0.79 (0.11)	0.60 (0.28)	0.19 (0.19)
Mendizabal et al. [6,41]	0.83 (0.12)	1.20 (1.03)	0.14 (0.17)	0.84 (0.08)	0.38 (0.26)	0.11 (0.12)						
Ciompi et al. [6,8]							0.76 (0.11)	1.78 (0.83)	0.17 (0.14)	0.84 (0.10)	0.57 (0.39)	0.12 (0.12)
Unal et al. [6,17]				0.81 (0.12)	0.47 (0.39)	0.14 (0.13)				0.76 (0.13)	0.64 (0.48)	0.21 (0.16)
Downe et al. [6,42]				0.77 (0.09)	0.47 (0.22)	0.15 (0.12)				0.74 (0.17)	0.76 (0.48)	0.23 (0.19)

the MA border, in the case of the non-artifact frames, the mean value of JM was equal to 0.9 and 0.87 in dataset A and B, respectively, with the standard deviation of smaller than 0.05 (Tables 2 and 3). The small value of the standard deviation of JM at both frame frequencies accounts for the robustness and generality of the proposed process in terms of selecting the MA border in the non-artifact images. Further, the proposed process can extract the lumen border in non-artifact frames in both datasets A and B with the precision close to the golden standard [6]. Similarly, the proposed process features the capability of high-reliability segmentation of the lumen and MA borders for the IVUS frames in the presence of plaque, stent, side vessel, guidewire, and catheter one vessel wall. Considering the bifurcation category, the proposed process is able to extract both lumen and MA borders reliably in the frames of dataset B, as well as the capability of acceptable extraction of the MA border in the frames of dataset A. Consequently, the worst case of the border detection process occurred in the bifurcation category. In terms of luminal measurement, the very high correlation of ALD in the proposed process with the manual border ($r = 0.94$), as well as that of LA in this process with the manual border ($r = 0.94$) indicated the high stability and accuracy of the proposed method in estimating the dimensions of the luminal area in dataset B. Similarly, the dimensions of the luminal area with the high correlation of ALD in the proposed process with the manual border ($r = 0.75$) was estimated in dataset A, along with the high correlation of LA in this process with the manual border ($r = 0.74$). Regarding the position error measurement, the MeanD lower than 0.5 mm and 0.17 mm for dataset A and B, respectively, indicates high accuracy of the proposed method in estimating positions of vessel walls. Regarding the wall thickness measurement, the mean WTE difference of lower than 0.37 (in case of the both datasets A and B), as well as the very high correlation of the obtained volume by the proposed process with the manually obtained volume (in case of the dataset B) confirmed the capability of the proposed method to use for the clinical aspects. Regarding the sensitivity, the OAT experiment indicates the important role of the search area of the proposed method to estimate the lumen and MA borders.

In order to compare the proposed method with those proposed in the previous studies, comparing the proposed method with those proposed for both datasets A and B, as well as the proposed method with all methods in previous studies were considered. Table 7 indicates the comparison, along with the positive and negative points. Since the time of the standard data was provided by Ref. [6], two general methods were proposed to date for both datasets A and B by Destrempes et al. [6,14] and Exarchos et al. [6]. Compared with Exarchos's method, the proposed method has a single negative point for dataset A and two positive points for the dataset B for the lumen border. In addition, regarding the MA border, the proposed method has one negative and two positive points for dataset A and B, respectively, compared with Exarchos's method. Therefore, it is clear that the proposed method has distinct superiority for both lumen and MA border detections in case of dataset B although Exarchos's method exhibits relative superiority for the dataset A. The semi-automatic method presented by Destrempes et al. [6,14] was recognized as the most efficient method in Ref. [6]. Regarding the comparison between the proposed method and [6,14], the superiority of its method in both datasets and both lumen and MA borders is obvious although it is limited by its semi-automatic nature. Comparing the proposed method with other methods in terms of the lumen border for the dataset A indicates its similarity with the method of Wang et al. [6], superiority over that of Alberti et al. [6], and weakness compared with Mendizabal-Ruiz et al. [6,41]. Further, in terms of detecting the lumen border in dataset B, the proposed method could exhibit its superiority over that of Wang et al. [6], Exarchos et al. [6], Downe et al. [6,42], Unal et al. [6,17] and weakness compared with Faraji et al. [16] and Jodas et al. [11]. Furthermore, the MA border detection for dataset A represents the superiority over that of Ciompi et al. [8] and weakness compared with Essa and Xie [15]. In addition, the proposed method was shown to have less accuracy only

Table 7
Statistical significance results for dataset A and B by using the paired *t*-test at 5%.

		Faraji et al. [16]	Essa et al. [15]	Jodas et al. [11]	Wang et al. [6]	Destrempes et al. [6,14]	Alberti et al. [6]	Exarchos et al. [6]	Mendizabal et al. [6,41]	Ciompi et al. [6,8]	Unal et al. [6,17]	Downe et al. [6,42]
Proposed Method	Lumen-A				N N N	- N -	+ N +	N N -	- N N			
	Media-A		- N N			- N N		- N N		N + +		
	Lumen-B	- - -		- - -	N + +	- - -	+ + +	+ + N	N N N		+ + +	+ + +
	Media-B	+ N +				- - -		+ N +		- - N	+ N +	+ + +

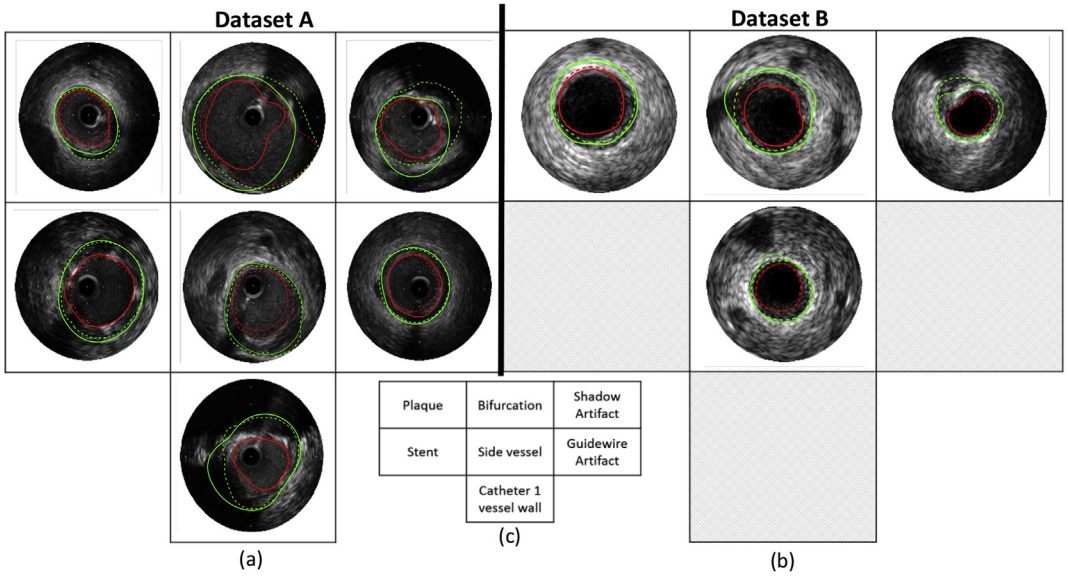

Fig. 16. MA (green) and lumen (red) borders of the frames with different categories in dataset A (a) and dataset B (b). (c) arrangement of the categories in (a) and (b) (The obtained borders by the proposed method and by an expert [6] are shown with the continuous and dashed curves, respectively).

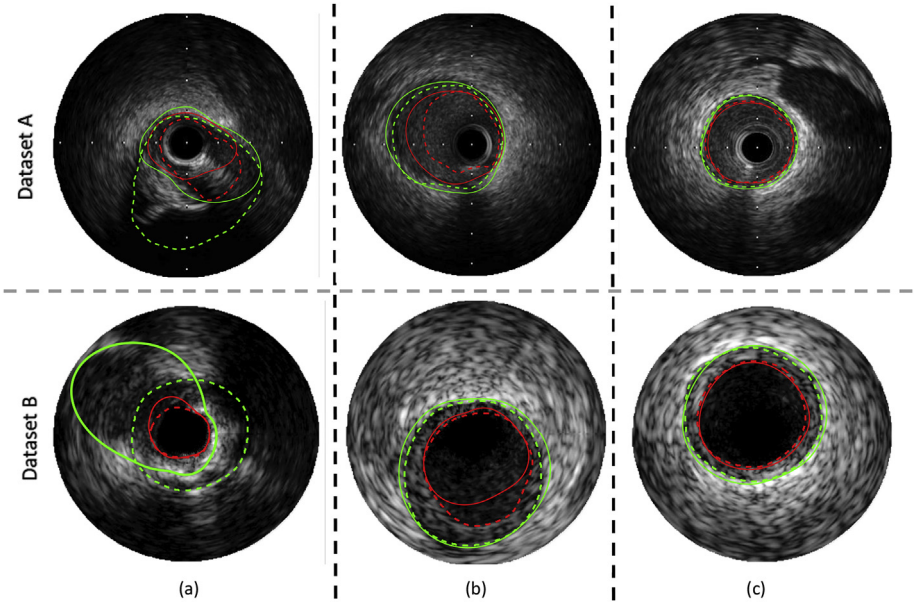

Fig. 17. MA (green) and lumen (red) borders of frames for dataset A (the first row) and dataset B (the second row): (a) *worst* performance, (b) *medium* performance, (c) *best* performance (The obtained borders by the proposed method and by an expert [6] are shown with continuous and dashed curves, respectively).

than that of Ciompi et al. [6,8], although it is superior to the method of Downe et al. [6,42], Faraji et al. [16], and Unal et al. [6,17] in terms of the MA border detection in case of dataset B.

In the frames with bifurcation, the MA border (and consequently lumen border) is not completely visible in the image due to the penetration depth limitation of the IVUS imaging. The proposed theory relies on such a problem. Regarding the proposed RWCV criterion, when there is no distinct border at the radius of the image, the uniformity of the RWCV at any point of the radius causes the radial threshold to incline toward the value equal to half of the image radius,

which results in occurring a cutting with high slope for the MA border within the border estimation process. Consequently, since the lumen border estimation is limited to the selected radius of MA border and due to the lack of a border in the region of interest, the lumen border inclines toward being half of the MA border radius. However, the proposed ad-hoc algorithm detects this sudden change in the border and estimates the correct border by removing the incorrect border and using interpolation. If a region with no clear border is large in relation to the entire image, a reduction occurs in the reliability of interpolation, which results in estimating the borders incorrectly (Fig. 16). Obviously, with regard to the sequential procedure of the proposed process, the sensitivity of the lumen border estimation in the images with bifurcation becomes higher than that of the MA border. Accordingly, the mean value of JM reduced by 0.64 for the lumen border in the images with bifurcation. Investigating this metric for the lumen and MA borders, along with the results presented in Fig. 16, indicates the effect of bifurcation dimensions on the accuracy of border extraction. First, it seems that the removal of a relatively large area by the ad-hoc algorithm and subsequent interpolation of that range occurs in other categories such as shadow artifact and stent. However, the proposed ad-hoc algorithm is reliable in such cases since the vessel geometry in these categories has a structure resembling a closed curve. Such a claim is confirmed by the mean JM values of 0.80 and 0.71 for the lumen and MA borders, respectively, in the stent category and the JM values of 0.77 and 0.72 for the lumen and MA borders, respectively, in the shadow artifact category for dataset A. Similarly, regarding dataset B, the mean JM values of 0.72 and 0.83 for the lumen and MA borders, respectively, were improved, compared with the values of 0.82 and 0.83 for the lumen and MA borders, respectively, before applying the ad-hoc algorithm.

Apart from the above-mentioned points, the major advantage of the proposed method lies in the proposed radial threshold theory. The proposed method, in addition to being automated, is capable of estimating the lumen and MA borders for each angle independently. Thus, the border search process can be implemented for a polar image in a parallel processing structure. In addition, the number of determinant angles of the border can be decreased or increased to control the processing load. Further, this method can be generalized to extract the borders in the IVUS longitudinal-mode images, which is widely used to register the IVUS sequences.

5. Conclusion

In the present study, a single-frame universal process was presented based on a new statistical method. For this purpose, a border search theory on the radial profile was proposed first in order to provide the independence of the border extraction process at any cutting angle from the other angles. This theory was based on a nonparametric statistical technique, which eventually led to the definition of a new threshold called “radial threshold”. Then, a three-step process based on this theory was proposed to extract the lumen and MA borders in the IVUS frames. The first step included preprocessing, the Cartesian-to-polar coordinates conversion, and removal of the artifact effects. During the second step, a sequential algorithm was proposed for the lumen and MA border extractions based on the proposed theory. Finally, an ad-hoc procedure was proposed for detecting, labeling, removing, and compensating the discontinuous borders.

The proposed method was evaluated in two stages by means of two datasets. The first dataset included the synthetic images similar to the structure of the IVUS image with the speckle noise for different PSNRs, which was used in evaluating the radial threshold theory and regularized criterion. The second dataset was a standard publicly available dataset acquired by two different 20 and 40 MHz probes by comparing the proposed method with those of previous studies. Based on the results, the proposed method was close to the best method for the frames acquired by the 40 MHz probes featuring an obvious superiority to the gold standard among all existing methods for the frames acquired by the 20 MHz probes.

Further studies can be conducted for developing the proposed method to extract the vessel walls of a sequence in the IVUS longitudinal-mode image. In addition, the proposed theory can be evaluated to segment the images having a radial profile such as intravascular optical coherence tomography (IVOCT) images.

Conflict of interest

None Declared

Funding sources

This research did not receive any specific grant from funding agencies in the public, commercial, or not-for-profit sectors.

Acknowledgment

The authors would like to thank Dr. Simone Balocco at the University of Barcelona for providing the labeling information on the existing artifacts in the dataset.

References

[1] N. Bom, C.T. Lancée, F.C. Van Egmond, An ultrasonic intracardiac scanner, Ultrasonics 10 (1972) 72–76, https://doi.org/10.1016/0041-624X(72)90250-8.

[2] G. Guagliumi, R. Virmani, The race to achieve the gold standard in coronary imaging, Rev. Española Cardiol. 62 (2009) 599–602 http://www.ncbi.nlm.nih.gov/pubmed/19480754.

[3] G.S. Mintz, S.E. Nissen, W.D. Anderson, S.R. Bailey, R. Erbel, P.J. Fitzgerald, F.J. Pinto, K. Rosenfield, R.J. Siegel, E.M. Tuzcu, American College of Cardiology clinical expert consensus document on standards for acquisition, measurement and reporting of intravascular ultrasound studies (ivus): a report of the american college of cardiology task force on clinical expert consensus documents developed in collaboration with the european society of cardiology endorsed by the society of cardiac angiography and interventions, J. Am. Coll. Cardiol. 37 (2001) 1478–1492.

[4] S.C. Smith, T.E. Feldman, J.W. Hirshfeld, A.K. Jacobs, M.J. Kern, S.B. King, D.A. Morrison, W.W. O'Neill, H.V. Schaff, P.L. Whitlow, D.O. Williams, Acc/aha/scai 2005 guideline update for percutaneous coronary intervention: a report of the American College of Cardiology/American Heart Association task force on practice guidelines (ACC/AHA/SCAI writing committee to update the 2001 guidelines for percut, Circulation 113 (2006) e166–e286, https://doi.org/10.1161/CIRCULATIONAHA.105.170815.

[5] A. Katouzian, E.D. Angelini, S.G. Carlier, J.S. Suri, N. Navab, A.F. Laine, A state-of-the-art review on segmentation algorithms in intravascular ultrasound (IVUS) images, IEEE Trans. Inf. Technol. Biomed. 16 (2012) 823–834, https://doi.org/10.1109/TITB.2012.2189408.

[6] S. Balocco, C. Gatta, F. Ciompi, A. Wahle, P. Radeva, S. Carlier, G. Unal, E. Sanidas, J. Mauri, X. Carillo, T. Kovarnik, C.-W. Wang, H.-C. Chen, T.P. Exarchos, D.I. Fotiadis, F. Destrempes, G. Cloutier, O. Pujol, M. Alberti, E.G. Mendizabal-Ruiz, M. Rivera, T. Aksoy, R.W. Downe, I.A. Kakadiaris, Standardized evaluation methodology and reference database for evaluating IVUS image segmentation, Comput. Med. Imag. Graph. 38 (2014) 70–90 https://doi.org/10.1016/j.compmedimag.2013.07.001.

[7] J.A. Noble, D. Boukerroui, Ultrasound image segmentation: a survey, IEEE Trans. Med. Imag. 25 (2006) 987–1010, https://doi.org/10.1109/TMI.2006.877092.

[8] F. Ciompi, O. Pujol, C. Gatta, M. Alberti, S. Balocco, X. Carrillo, J. Mauri-ferre, P. Radeva, HoliMAb: a holistic approach for Media – adventitia border detection in intravascular ultrasound, Med. Image Anal. 16 (2012) 1085–1100, https://doi.org/10.1016/j.media.2012.06.008.

[9] L. Lo Vercio, J.I. Orlando, M. del Fresno, I. Larrabide, Assessment of image features for vessel wall segmentation in intravascular ultrasound images, Int. J. Comput. Assist. Radiol. Surg. 11 (2016) 1397–1407, https://doi.org/10.1007/s11548-015-1345-4.

[10] S. Su, Z. Hu, Q. Lin, W.K. Hau, Z. Gao, H. Zhang, An artificial neural network method for lumen and media-adventitia border detection in IVUS, Comput. Med. Imag. Graph. 57 (2017) 29–39, https://doi.org/10.1016/j.compmedimag.2016.11.003.

[11] D.S. Jodas, A.S. Pereira, J.M.R.S. Tavares, Automatic segmentation of the lumen region in intravascular images of the coronary artery, Med. Image Anal. 40 (2017) 60–79, https://doi.org/10.1016/j.media.2017.06.006.

[12] G.D. Giannoglou, Y.S. Chatzizisis, V. Koutkias, I. Kompatsiaris, M. Papadogiorgaki, V. Mezaris, E. Parissi, P. Diamantopoulos, M.G. Strintzis, N. Maglaveras, G.E. Parcharidis, G.E. Louridas, A novel active contour model for fully automated segmentation of intravascular ultrasound images: in vivo validation in human coronary arteries, Comput. Biol. Med. 37 (2007) 1292–1302, https://doi.org/10.1016/j.compbiomed.2006.12.003.

[13] F.S. Zakeri, S.K. Setarehdan, S. Norouzi, Automatic media-adventitia IVUS image segmentation based on sparse representation framework and dynamic directional active contour model, Comput. Biol. Med. 89 (2017) 561–572, https://doi.org/10.1016/j.compbiomed.2017.03.022.
[14] F. Destrempes, M.-H. Roy Cardinal, L. Allard, J.-C. Tardif, G. Cloutier, Segmentation method of intravascular ultrasound images of human coronary arteries, Comput. Med. Imag. Graph. 38 (2014) 91–103, https://doi.org/10.1016/j.compmedimag.2013.09.004.
[15] E. Essa, X. Xie, Automatic segmentation of cross-sectional coronary arterial images, Comput. Vis. Image Understand. 165 (2017) 97–110, https://doi.org/10.1016/j.cviu.2017.11.004.
[16] M. Faraji, I. Cheng, I. Naudin, A. Basu, Segmentation of arterial walls in intravascular ultrasound cross-sectional images using extremal region selection, Ultrasonics 84 (2018) 356–365, https://doi.org/10.1016/j.ultras.2017.11.020.
[17] G. Unal, S. Bucher, S. Carlier, G. Slabaugh, T. Fang, K. Tanaka, Shape-driven segmentation of the arterial wall in intravascular ultrasound images, IEEE Trans. Inf. Technol. Biomed. 12 (2008) 335–347, https://doi.org/10.1109/TITB.2008.920620.
[18] D. China, P. Mitra, D. Sheet, Segmentation of Lumen and External Elastic Laminae in Intravascular Ultrasound Images Using Ultrasonic Backscattering Physics Initialized Multiscale Random Walks BT - Computer Vision, Graphics, and Image Processing, Springer International Publishing, Cham, 2017, pp. 393–403.
[19] T. Loupas, W.N. McDicken, P.L. Allan, An adaptive weighted median filter for speckle suppression in medical ultrasonic images, IEEE Trans. Circ. Syst. 36 (1989) 129–135.
[20] N. Otsu, A threshold selection method from gray-level histograms, IEEE Trans. Syst. Man. Cybern. 9 (1979) 62–66, https://doi.org/10.1109/TSMC.1979.4310076.
[21] Z. Hou, Q. Hu, W.L. Nowinski, On minimum variance thresholding, Pattern Recogn. Lett. 27 (2006) 1732–1743, https://doi.org/10.1016/j.patrec.2006.04.012.
[22] J. Fan, F. Zhao, Two-dimensional Otsu's curve thresholding segmentation method for gray-level images, Acta Electron. Sin. 35 (2007) 751.
[23] F. Nie, Y. Wang, M. Pan, G. Peng, P. Zhang, Two-dimensional extension of variance-based thresholding for image segmentation, Multidimens. Syst. Signal Process. 24 (2013) 485–501, https://doi.org/10.1007/s11045-012-0174-7.
[24] S.U. Lee, S.Y. Chung, R.H. Park, A comparative performance study of several global thresholding techniques for segmentation, Comput. Vis. Graph Image Process 52 (1990) 171–190 https://doi.org/10.1016/0734-189X(90)90053-X.
[25] H.-F. Ng, Automatic thresholding for defect detection, Pattern Recogn. Lett. 27 (2006) 1644–1649 https://doi.org/10.1016/j.patrec.2006.03.009.
[26] X.C. Yuan, L.S. Wu, Q. Peng, An improved Otsu method using the weighted object variance for defect detection, Appl. Surf. Sci. 349 (2015) 472–484, https://doi.org/10.1016/j.apsusc.2015.05.033.
[27] Z. Li, C. Liu, G. Liu, Y. Cheng, X. Yang, C. Zhao, A novel statistical image thresholding method, AEU - Int. J. Electron. Commun. 64 (2010) 1137–1147, https://doi.org/10.1016/j.aeue.2009.11.011.
[28] J.H. Xue, D.M. Titterington, T-Tests, F-Tests and Otsu's methods for image thresholding, IEEE Trans. Image Process. 20 (2011) 2392–2396, https://doi.org/10.1109/TIP.2011.2114358.
[29] H. Sofian, J.C.M. Than, N.M. Noor, H. Dao, Segmentation and detection of media adventitia coronary artery boundary in medical imaging intravascular ultrasound using otsu thresholding, BioSignal Anal. Process. Syst. (ICBAPS), 2015 Int. Conf, IEEE, 2015, pp. 72–76.
[30] J.D.N. Cheeke, Fundamental and Applications of Ultrasonic Waves, CRC Press, 2002.
[31] M. Rosales, P. Radeva, J.S. Suri, D.L. Wilson, S. Laxminarayan (Eds.), A Basic Model for IVUS Image Simulation BT - Handbook of Biomedical Image Analysis: Volume I: Segmentation Models Part A, Springer US, Boston, MA, 2005, pp. 1–55, , https://doi.org/10.1007/0-306-48551-6_1.
[32] O. Demirkaya, M.H. Asyali, P.K. Sahoo, Image Processing with {MATLAB}: Applications in Medicine and Biology, CRC Press, 2008.
[33] C. De Boor, A Practical Guide to Splines, Springer-Verlag, New York, 1978.
[34] S.S. Young, Computerized Data Acquisition and Analysis for the Life Sciences, (2001), https://doi.org/10.1017/CBO9780511609558.
[35] H. Alt, M. Godau, Computing the Fréchet distance between two polygonal curves, Int. J. Comput. Geom. Appl. 5 (1995) 75–91, https://doi.org/10.1142/S0218195995000064.
[36] E.L. Lehmann, Elements of Large Sample Theory, Springer Science & Business Media, 2004.
[37] I.D.J. Bross, Critical levels, statistical language and scientific inference, Found. Stat. Inference (1971) 500–513.
[38] D. Gil, A. Hernandez, O. Rodriguez, J. Mauri, P. Radeva, Statistical strategy for anisotropic adventitia modelling in IVUS, IEEE Trans. Med. Imag. 25 (2006) 768–778.
[39] M. Sonka, X. Zhang, M. Siebes, R.R. Chada, C.R. McKay, S.M. Collins, Automated detection of wall and plaque borders in intravascular ultrasound images, Med. Imaging 1994 Physiol. Funct. from Multidimens. Images, International Society for Optics and Photonics, 1994, pp. 13–23.
[40] C. Daniel, One-at-a-time plans, J. Am. Stat. Assoc. 68 (1973) 353–360.
[41] E.G. Mendizabal-Ruiz, M. Rivera, I.A. Kakadiaris, Segmentation of the luminal border in intravascular ultrasound B-mode images using a probabilistic approach, Med. Image Anal. 17 (2013) 649–670, https://doi.org/10.1016/j.media.2013.02.003.
[42] R. Downe, Segmentation of intravascular ultrasound images using graph search and a novel cost function, MICCAI Work. CVII. (2008) 71–79.